PR12-13-010

(Proposal to Jefferson Lab PAC 40)

Exclusive Deeply Virtual Compton and Neutral Pion Cross-Section Measurements in Hall C

(Dated: May 6, 2013)

We propose to use the High Momentum Spectrometer of Hall C combined with a $PbWO_4$ electromagnetic calorimeter in order to perform high precision measurements of the Deeply Virtual Compton Scattering (DVCS) cross section. A wide range of kinematics accessible with an 11 GeV electron beam off an unpolarized proton target will be covered. The azimuthal, energy and helicity dependences of the cross section will all be exploited in order to separate the interference and $DVCS^2$ contributions to each of the Fourier moments of the cross section. For each term, its Q^2 dependence will be measured independently. At the same time, the exclusive π^0 electroproduction cross section will also be measured and a longitudinal/transverse separation will be performed. The total request is for 65 days of beam.

A. Camsonne, S. Covrig, R. Ent, D. Gaskell, F.X. Girod, M. Jones,

C. Keppel, P. Nadel-Turoński, A. J. R. Puckett, B. Sawatzky,

P. Solvignon, S.A. Wood, B. Wojtsekhowski

Jefferson Lab, Newport News, VA 23606

A. Asaturyan, A. Mkrtchyan, H. Mkrtchyan, V. Tadevosyan, S. Zhamkochyan

A.I. Alikhanyan National Science Laboratory, Yerevan 0036, Armenia

M. Boer, C. Desnault, R. Dupré, B. Garillon, M. Guidal, M. Hattawy, H.S. Jo,

A. Martí Jimenez-Argüello, C. Muñoz Camacho[†*] , S. Niccolai, R. Paremuzyan[*]

Institut de Physique Nucleaire d'Orsay, IN2P3, BP 1, 91406 Orsay, France

M. Defurne, M. Garçon, F. Sabatié

SPhN (Saclay), CEA/DSM/IRFU, Gif-sur-Yvette, France

I. Albayrak, M. Carmignotto, J. Dénes-Couto, N. Hlavin, T. Horn[*],

F. Klein, B. Nepal

The Catholic University of America, Washington, DC 20064

M. Canan, C. Hyde[*], M.N.H. Rashad

Old Dominion University, Norfolk, Virginia

P. King, J. Roche[*]

Ohio University, Athens, OH 45701

[*] Co-spokesperson

[†] Contact person: munoz@ipno.in2p3.fr

M. Ben Ali, L. Ghedira, M. Mazouz,

Faculté des Sciences de Monastir, Département de physique, 5000-Monastir, Tunisia

A. Fradi

Faculty of Sciences of Gabes, Department of Physics, 6072-Gabes, Tunisia

D. Day, D. Keller, O. Rondon

University of Virginia, Charlottesville, VA, USA

J.R.M. Annand, D.J. Hamilton

University of Glasgow, Glasgow, Scotland, UK

S. Sirca

University of Ljubljana, Ljubljana, Slovenia

M. Elaasar

Southern University at New Orleans

G. Huber

Univ. of Regina, Regina, SK S4S0A2, Canada

F. Wesselmann

Xavier University of Louisiana, New Orleans

P. E. C. Markowitz

Florida International University, Miami, FL 33199, USA

A. Ahmidouch, S. Danagoulian

North Carolina A&T State University, USA

M. H. Shabestari

Mississippi State University, USA

D. Androic

Faculty of Science, University of Zagreb

C. Chen, Y. Han, P. Gueye, L. Tang

Hampton University, Hampton, VA 23668, USA

V. Sulkosky

Massachusetts Institute of Technology, Cambridge, Massachusetts 02139, USA

NEUTRAL PARTICLE SPECTROMETER (NPS) COLLABORATION

Contents

I. Introduction 4

II. Physics goals 6

A. Energy dependence of the DVCS cross section 8

B. DVCS kinematic extension: high Q^2 and low x_B 10

C. Exclusive π^0 production cross-section: L/T separation 11

III. Experimental setup 14

A. High Momentum Spectrometer 14

B. Photon detection: the neutral particle spectrometer 15

The $PbWO_4$ electromagnetic calorimeter 17

C. Beam pipe and angle coverage 21

D. Exclusivity of the DVCS and π^0 reactions 23

E. Systematics uncertainties 25

IV. Proposed kinematics and projections 26

V. Background studies 30

VI. Summary 33

A. DVCS Formalism 34

References 36

I. INTRODUCTION

Deeply Virtual Compton Scattering (DVCS) refers to the reaction $\gamma^* p \to p\gamma$ in the Bjorken limit of Deep Inelastic Scattering (DIS). Experimentally, we can access DVCS through electroproduction of real photons $ep \to ep\gamma$, where the DVCS amplitude interferes with the so-called Bethe-Heitler (BH) process. The BH contribution is calculable in QED since it corresponds to the emission of the photon by the incoming or the outgoing electron.

DVCS is the simplest probe of a new class of light-cone (quark) matrix elements, called Generalized Parton Distributions (GPDs). The GPDs offer the exciting possibility of the first ever spatial images of the quark waves inside the proton, as a function of their wavelength [1–6]. The correlation of transverse spatial and longitudinal momentum information contained in the GPDs provides a new tool to evaluate the contribution of quark orbital angular momentum to the proton spin.

GPDs enter the DVCS cross section through integrals, called Compton Form Factors (CFFs). CFFs are defined in terms of the vector GPDs H and E, and the axial vector GPDs $\tilde{H}$ and $\tilde{E}$. For example ($f \in \{u, d, s\}$) [7]:

$$\mathcal{H}(\xi,t) \;=\; \sum_f \left[\frac{e_f}{e}\right]^2 \Bigg\{ i\pi \left[H_f(\xi,\xi,t) - H_f(-\xi,\xi,t)\right] + \mathcal{P}\int_{-1}^{+1} dx \left[\frac{1}{\xi - x} - \frac{1}{\xi + x}\right] H_f(x,\xi,t) \Bigg\}. \tag{1}$$

Thus, the imaginary part accesses GPDs along the line $x = \pm\xi$, whereas the real part probes GPD integrals over x. The 'diagonal' GPD, $H(\xi,\xi,t=\Delta^2)$ is not a positive-definite probability density, however it is a transition density with the momentum transfer $\Delta_\perp$ Fourier-conjugate to the transverse distance r between the active parton and the center-of-momentum of the spectator partons in the target [8]. Furthermore, the real part of the Compton Form Factor is determined by a dispersion integral over the diagonal $x = \pm\xi$ plus the D-term [9–12]:

$$\Re\mathrm{e}\left[\mathcal{H}(\xi,t)\right] = \int_{-1}^{1} dx \left\{ \left[H(x,x,t) + H(-x,x,t)\right] \left[\frac{1}{\xi - x} - \frac{1}{\xi + x}\right] + 2\frac{D(x,t)}{1-x} \right\} \tag{2}$$

The D-term [13] only has support in the ERBL region $|x| < \xi$ in which the GPD is determined by $q\overline{q}$ exchange in the t-channel.

Extractions of GPDs is a much more demanding task than the extraction of Parton Distribution Functions (PDF) or Form Factors (FF) due to the complex functional structures of GPDs. Moreover, we need to extract four functions H, E, $\widetilde{H}$ and $\widetilde{E}$ of three variables (x, ξ, t) for each quark flavor (u, d and s). The Q^2-dependence is governed by the QCD evolution equations. Building a flexible yet robust GPD parameterization is very involved and the problem is still open today, but several groups have made attempts to fit GPDs (or CFFs) to data during the last few years. A recent extensive review on the subject can be found in [14]. We describe the different fitting methods below.

- Local fits of CFFs

  The first approach, pioneered in [15] and used in [16–19] assumes the independence of the real and imaginary parts of CFFs. The main assumptions are the validity of the twist-2 leading order analysis of existing DVCS measurements and a negligible contribution of $\mathrm{Im}\,\tilde{\mathcal{E}}$. Each kinematic bin (x_B, t, Q^2) is taken independently of the others, and the seven values $\mathrm{Re}\,\mathcal{H}$, $\mathrm{Im}\,\mathcal{H}$, $\mathrm{Re}\,\mathcal{E}$, $\mathrm{Im}\,\mathcal{E}$, $\mathrm{Re}\,\widetilde{\mathcal{H}}$, $\mathrm{Im}\,\widetilde{\mathcal{H}}$ and $\mathrm{Re}\,\widetilde{\mathcal{E}}$ are extracted simultaneously. This method has the clear advantage of being almost model-independent but the problem is often under-constrained. In the following we will refer to these fits as *local fits*.

- Global fits of GPDs

  In the spirit of the work done on PDFs and FFs, *global fits* require a physically motivated parameterization of GPDs and deal with all observables on all kinematic bins at once. The main advantage is obvious : the ability to extrapolate outside of the data region, and therefore evaluate for instance Ji's sum rule ($t \to 0$) or more generally, study the 3D partonic structure of the nucleon ($\xi \to 0$). The free coefficients entering the expressions for GPDs are determined from PDFs, FFs and from DVCS data. Several such studies have been reported recently for DVCS [20–22]. Note that fixed-t dispersion relations are used as a key ingredient in [20]. While currently most of global fits assume leading order expressions for the DVCS amplitude, calculations at next to leading order in the strong coupling constant have recently been published [23].

- Hybrid fits of GPDs

  The *hybrid* fitting procedure used in [16] is a combination of the previous two methods and has been applied with the main assumption of H-dominance and twist-2 accuracy.

It involves a parameterization which fulfills the polynomiality condition of GPDs and includes Q^2 evolution at leading order in α_S. Since this function is otherwise arbitrary, its specific form is *a posteriori* validated by the quality of the fit. It makes it hazardous to extrapolate the extracted GPD outside the fitting domain as unphysical oscillations may occur. The model dependence is tested by a systematic comparison to local fits and an estimate of the systematic error induced by the H-dominance hypothesis. The good agreement of the local fits with respect to the global fits is a strong consistency check of this approach.

- Neural network fits of GPDs

  Neural network fits had been successfully performed for PDFs but their use for GPD extraction is quite recent. First results are described in [24] within the H-dominance assumption. Although it is too early to judge the advantages and shortcomings of this approach, it is worth noting that it is a new development in the field of GPD extraction.

In conclusion, the first extractions of GPDs or CFFs from early JLab and HERMES DVCS data are encouraging and a lot of progress has been made by the different groups involved. The abundance of 11 GeV data will allow for more flexible functional forms to be fitted, which will help to relax the drastic hypothesis made so far such as H-dominance, twist-2 dominance and leading order analysis. There is no doubt that in the coming years, several groups will refine their fitting machinery and will get ready to analyze a large quantity of data from the Jefferson Lab upgrade.

II. PHYSICS GOALS

In this experiment we propose to exploit the full kinematical dependence of the DVCS cross section in order to isolate all Fourier moments of the cross-section on an unpolarized target and separate the DVCS-BH interference and DVCS^2 contributions to each of them. Each individual term has a distinct Q^2 dependence that we will measure and will allow us to quantify the size of higher-twist corrections. Notice that so far only the Q^2-dependence of the imaginary part of the DVCS amplitude has been studied experimentally [25]. While the data showed indications of leading twist dominance, the test on several other observables

including the real part of the DVCS amplitude will confirm this observation. Notice that a precise study of Q^2–dependences and higher twists are both necessary and very interesting from the physics point of view. On the one hand, recent calculations [26] show that finite–t and target mass corrections to DVCS are significant at JLab kinematics. On the other hand, twist-three GPDs can give access to a longitudinal proton spin sum rule [27] in a similar way as twist-2 GPDs probe the transverse spin through the well-know Ji sum rule [2].

The kinematical dependences mentioned above include the azimuthal dependence of the cross section as a function of the angle $\phi_{\gamma\gamma}$ between the leptonic and hadronic planes, and also the beam energy dependence of the cross section in a way similar to a Rosenbluth measurement. Lastly, the beam helicity dependence of the cross section will also be exploited in order to isolate the imaginary part and the real part of the DVCS amplitude.

We propose to extend the high precision DVCS cross-section measurements performed at 6 GeV to a much extended kinematical domain accessible by a 11 GeV beam. An experiment that will initiate this extension at 11 GeV has already been approved in Hall A (E12-06-114) [28]. However, the limited momentum reach of Hall A spectrometer ($< 4\,\mathrm{GeV/c}$) limits the physics reach of the Hall A kinematics. This proposal intends to expand the physics impact in three distinct ways:

- Complement the kinematic settings of Hall A, by one or two conjugate setting (same Q^2 and x_B) at different beam energies. This will allow an L/T separation of the cross section, which for DVCS allows a separation of the $|\mathrm{DVCS}|^2$ term from the real part of the DVCS-BH interference. This energy separation is key to the overall DVCS program. Experiment E07-007 [29] will perform this separation at 6 GeV kinematics, but at 11 GeV this can only be performed in Hall C due to the high momentum of scattered electrons.

- Increase the Q^2 reach to even higher values at fixed x_B. This is essential in order to confirm the applicability of the GPD formalism to DVCS at Jefferson Lab. It will also allow to better quantify and understand higher-twist effects. Only with the high luminosity proposed in this experiment we can reach good statistical precision at high Q^2 and high x_B. While CLAS12 will perform measurements in these kinematics, the statistical precision will be limited in this region. However, it is in this particular region where we expect DVCS cross section to most deviate from Bethe-Heitler, making it

the particularly interesting for GPD studies.

- Expand the kinematic coverage to smaller values of x_B. High precision cross sections at low x_B can be used for comparison with other experimental data such as the one available from CLAS [30, 31] and the future CLAS12 [32, 33], as well the projected data from COMPASS at CERN [34]. The high counting rates of the low-x_B settings make this extension relatively inexpensive. In addition, the low x_B region is where CLAS and CLAS12 will have comparable statistical precision, making this a very valuable cross-check of very different experimental setups.

In conclusion, the proposed measurements will provide the highest precision data in the kinematic domain accessible with a 11 GeV beam, in order to extract all possible independent observables on an unpolarized proton target.

A. Energy dependence of the DVCS cross section

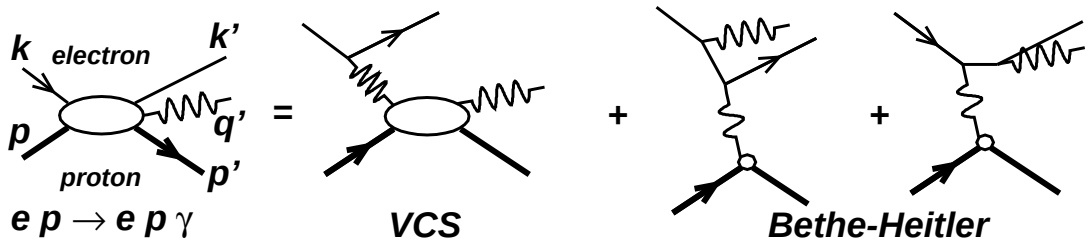

FIG. 1: Lowest order QED amplitude for the $ep \to ep\gamma$ reaction. The momentum four-vectors of all external particles are labeled at left. The net four-momentum transfer to the proton is $\Delta_\mu = (q - q')_\mu = (p' - p)_\mu$. In the virtual Compton scattering (VCS) amplitude, the (spacelike) virtuality of the incident photon is $Q^2 = -q^2 = -(k - k')^2$. In the Bethe-Heitler (BH) amplitude, the virtuality of the incident photon is $-\Delta^2 = -t$. Standard (e, e') invariants are $s_e = (k + p)^2$, $x_{\rm B} = Q^2/(2q \cdot p)$ and $W^2 = (q + p)^2$.

The photon electroproduction cross section of a polarized lepton beam of energy k off an unpolarized target of mass M is sensitive to the coherent interference of the DVCS amplitude with the Bethe-Heitler amplitude (see Fig. 1). It can be written as:

$$\frac{d^5\sigma(\lambda, \pm e)}{d^5\Phi} \;=\; \frac{d\sigma_0}{dQ^2 dx_B} \left|\mathcal{T}^{BH}(\lambda) \pm \mathcal{T}^{DVCS}(\lambda)\right|^2 / |e|^6$$

$$= \frac{d\sigma_0}{dQ^2 dx_B}\left[\left|\mathcal{T}^{BH}(\lambda)\right|^2 + \left|\mathcal{T}^{DVCS}(\lambda)\right|^2 \mp \mathcal{I}(\lambda)\right]\frac{1}{e^6} \quad (3)$$

$$\frac{d\sigma_0}{dQ^2 dx_B} = \frac{\alpha^3_{\rm QED}}{16\pi^2(s_e - M^2)^2 x_B}\frac{1}{\sqrt{1+\epsilon^2}} \quad (4)$$

$$\epsilon^2 = 4M^2 x_B^2/Q^2$$

$$s_e = 2Mk + M^2$$

where $d^5\Phi = dQ^2 dx_B d\phi_e dt d\phi_{\gamma\gamma}$, λ is the electron helicity and the $+(-)$ stands for the sign of the charge of the lepton beam. The BH contribution is calculable in QED, given our $\approx 1\%$ knowledge of the proton elastic form factors at small momentum transfer. The other two contributions to the cross section, the interference and the DVCS^2 terms, provide complementary information on GPDs. It is possible to exploit the structure of the cross section as a function of the angle $\phi_{\gamma\gamma}$ between the leptonic and hadronic plane to separate up to a certain degree the different contributions to the total cross section [35]. The angular separation can be supplemented by an energy separation. This energy separation is one of the goals of this proposal.

The $|\mathcal{T}^{BH}|^2$ term is given in [7], Eq. (25), and only its general form is reproduced here:

$$|\mathcal{T}^{BH}|^2 = \frac{e^6}{x_B^2 t y^2(1+\epsilon^2)^2\mathcal{P}_1(\phi_{\gamma\gamma})\mathcal{P}_2(\phi_{\gamma\gamma})}\sum_{n=0}^{2} c_n^{BH}\cos(n\phi_{\gamma\gamma}) \quad (5)$$

The harmonic terms c_n^{BH} depend upon bilinear combinations of the ordinary elastic form factors $F_1(t)$ and $F_2(t)$ of the proton. The factors $\mathcal{P}_i$ are the electron propagators in the BH amplitude [7].

The interference term in Eq. 3 is a linear combination of GPDs, whereas the DVCS^2 term is a bilinear combination of GPDs. These terms have the following harmonic structure:

$$\mathcal{I} = \frac{e^6}{x_B y^3 \mathcal{P}_1(\phi_{\gamma\gamma})\mathcal{P}_2(\phi_{\gamma\gamma}) t}\left\{c_0^{\mathcal{I}} + \sum_{n=1}^{3}\left[c_n^{\mathcal{I}}(\lambda)\cos(n\phi_{\gamma\gamma}) - \lambda s_n^{\mathcal{I}}\sin(n\phi_{\gamma\gamma})\right]\right\} \quad (6)$$

$$\left|\mathcal{T}^{DVCS}(\lambda)\right|^2 = \frac{e^6}{y^2 Q^2}\left\{c_0^{DVCS} + \sum_{n=1}^{2}\left[c_n^{DVCS}\cos(n\phi_{\gamma\gamma}) + \lambda s_n^{DVCS}\sin(n\phi_{\gamma\gamma})\right]\right\} \quad (7)$$

The $c_0^{DVCS,\mathcal{I}}$ and $(c,s)_1^{\mathcal{I}}$ harmonics are dominated by twist-two GPD terms, although they do have twist-three admixtures that must be quantified by the Q^2-dependence of each harmonic. The $(c,s)_1^{DVCS}$ and $(c,s)_2^{\mathcal{I}}$ harmonics are dominated by twist-three matrix elements, although

the same twist-two GPD terms also contribute (but with smaller kinematic coefficients than in the lower Fourier terms). The $(c,s)_2^{DVCS}$ and $(c,s)_3^{\mathcal{I}}$ harmonics stem from twist-two double helicity-flip gluonic GPDs alone. They are formally suppressed by α_s and will be neglected here. They do not mix, however, with the twist-two quark amplitudes. The exact expressions of these harmonics in terms of the quark Compton Form Factors (CFFs) of the nucleon are given in [36] and described in Appendix A.

An essential feature of Eqs. 6 and 7 is the incident beam energy dependence (at fixed Q^2, $\nu = Q^2/(2Mx_{\rm B})$):

$$\begin{aligned} \mathcal{I} &\propto 1/y^3 = (k/\nu)^3, \quad \text{and} \\ \left|\mathcal{T}^{DVCS}\right|^2 &\propto 1/y^2 = (k/\nu)^2. \end{aligned} \tag{8}$$

The lepton propagators of Eq. 6 as well as the $(c,s)_n$ harmonics contain additional beam energy dependences. It is primary goal of this experiment to exploit this energy dependence to separate the interference and DVCS-squared contributions to each of the Fourier terms.

As detailed in Appendix A, at leading twist there are 7 independent GPD terms:

$$\left\{\Re\mathrm{e}, \Im\mathrm{m}\left[\mathcal{C}^{\mathcal{I}}, \mathcal{C}^{\mathcal{I},V}, \mathcal{C}^{\mathcal{I},A}\right](\mathcal{F})\right\}, \qquad \text{and} \qquad \mathcal{C}^{DVCS}(\mathcal{F}, \mathcal{F}^*). \tag{9}$$

The azimuthal $\phi_{\gamma\gamma}$ dependence of the cross section provides 5 independent observables ($\sim$1, $\sim \cos\phi_{\gamma\gamma}, \sim \sin\phi_{\gamma\gamma}$ and $\sim \cos(2\phi_{\gamma\gamma}), \sim \sin(2\phi_{\gamma\gamma})$). The measurement of the cross section at two or more beam energies for exactly the same $Q^2, x_{\rm B}, t$ kinematics, provides the additional information in order to extract all leading twist observables independently. By studying their Q^2 dependence, we will be able to quantify higher twist contributions to each of them. Increasing the coverage both to larger Q^2 (next section) and to three beam energies (where feasible) will reduce the uncertainty of the extracted coefficients and provide a more stringent test of their Q^2 dependence. The third energy points are important because of the complicated energy dependencies of the kinematic coefficients. The sensitivity of our measurements to the energy dependence is illustrated in section IV.

B. DVCS kinematic extension: high Q^2 and low x_B

GPD measurements at Jefferson Lab rely on the assumption that deep exclusive reactions are well described by their leading twist mechanism. Theoretically this is true at high values

of Q^2. The value of Q^2 at which this approximation is valid experimentally needs to be determined and the contributions of higher twists to observables need to be quantified. The Q^2 dependence of cross sections is the most direct way to separate higher twist contributions to DVCS and other exclusive channels.

We propose to extend the measurements that will be performed in Hall A to higher Q^2 in Hall C for each value of x_B. Thus, we propose 3 additional settings at high Q^2 at $x_B = 0.36$, 0.5 and 0.6 respectively. Each of these settings require small angle settings for the calorimeter. These measurements are enabled by the proposed 0.3 Tesla-m sweep magnet between the target and the calorimeter. These settings will increase the lever arm in Q^2 by $\sim$40% at each value of x_B, allowing a much more stringent test of the Q^2 dependence of each separated observable in the DVCS cross section.

A full mapping of the GPDs requires data over a full range in x_B. The 11 GeV beam energy limits the low range in x_B that can be accessed at JLab in the DIS regime. Nonetheless, the high luminosity and low systematic errors of the Hall C setup will allow us to extend the kinematic range down to $x_B = 0.2$. These data will provide an important complement to the CLAS and HERMES data and future COMPASS and CLAS12 data. We propose four data points at $x_B = 0.2$, with $Q^2 = 2.0$ and $3.0\,\mathrm{GeV}^2$, and several beam energies (see Table III).

C. Exclusive π^0 production cross-section: L/T separation

While DVCS is the main goal of this proposal, exclusive π^0 events will be detected along with DVCS in our experimental setup. Pseudo-scalar mesons provide a very interesting and complementary insight into GPDs of the nucleon. The first cross section measurements for exclusive π^0 electroproduction in the valence region were performed in Hall A [37] with high precision, and complemented later in a much larger kinematic domain by the CLAS collaboration [38]. Both these datasets were not L/T separated, but provided clear evidence for strong contributions from transversely polarized virtual photons. This observation is in sharp contrast to the handbag factorization, which tells us that for asymptotically large photon virtualities, (Q^2), longitudinally polarized photons dominate [39, 40]. According to the handbag approach, the amplitudes for transverse photons are suppressed $\sim 1/Q$ as compared to those from longitudinal photons. The experimental evidence for strong

transverse virtual photon transitions comes from the CLAS π^+ data [41] and from the $\sin\phi_s$ harmonics measured with a transversally polarized target by HERMES [42]. Moreover, the CLAS [38] and Hall A measurements [37] of the π^0 cross sections reveal a transverse-transverse interference cross section that amounts to a substantial fraction of the unseparated cross section. Evidence for significant L-T interference in π^0 production also comes from CLAS beam spin asymmetries measurements [43]. In addition, a large contribution of the transverse cross section was observed in separated charged pion cross section data [44].

It has been argued in [45, 46] that, within the handbag approach, the π^0 electroproduction amplitudes for transversely polarized virtual photons are determined by transversity GPDs, in particular of H_T and $\tilde{E}_T$=$2H_T$ + E_T [47, 48]. On the one hand, the amplitudes for transversely polarized photons are parametrically suppressed by μ_π/Q as compared to the asymptotically leading amplitudes for longitudinally polarized photons (related to the usual GPDs $\widetilde{H}$ and $\widetilde{E}$). On the other hand, the parameter μ_π is fixed by the divergence of the axial-vector current, $\mu_\pi \approx 2$ GeV (at a scale of 2 GeV). This would suggest that there is no strong suppression of the transverse amplitudes at values of Q^2 accessible in present-day experiments. It is thus of great interest to determine the relative longitudinal and transverse contributions to the π^0 cross section.

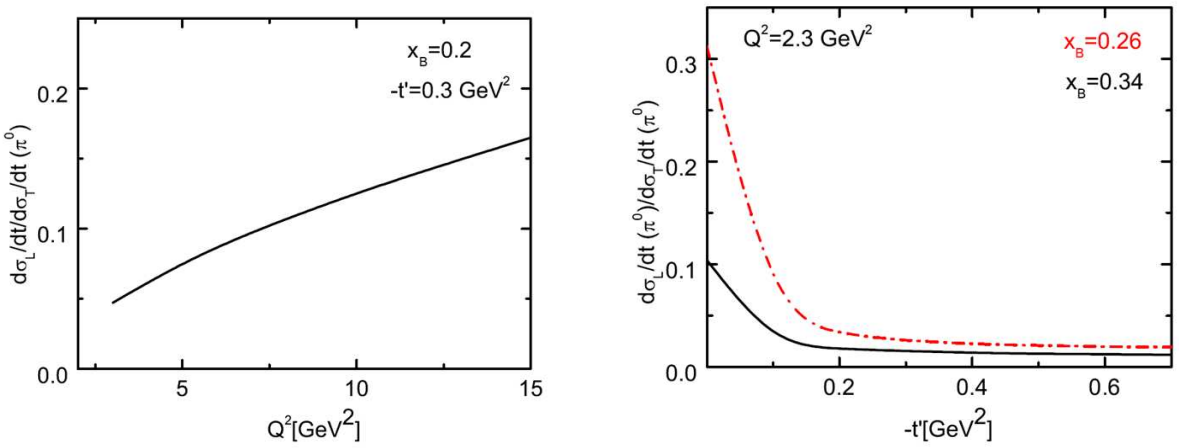

FIG. 2: The ratio of the longitudinal and transverse cross section for π^0 electroproduction. The predictions are taken from [49] and are based on [46].

In order to evaluate the amplitudes, the transversity GPDs are modeled with the help of the double-distribution ansatz. The pertinent parameters are fixed by fitting the HERMES data on π^+ electroproduction and by lattice QCD results [50]. Model predictions are shown in Fig. 2. One should bear in mind that these estimates could have uncertainties of about

at least a factor of two [49]. In order to determine the transversity GPDs, more precise data on π^0 (and on other pseudoscalar meson) electroproduction at larger values of Q^2 and W, than available from JLab at 6 GeV, are needed.

A particularly clean probe of large transversity effects in pion electroproduction is the measurement of the relative contribution of σ_L and σ_T to the cross section as a function of Q^2. However, there are currently no L/T separated π^0 data available above the resonance region and theoretical predictions have large uncertainties. This emphasizes the need to experimentally determine the longitudinal and transverse cross sections (or put a boundary on their values). The first π^0 L/T separated data will come from Hall A experiments E07-007 [29] off the proton and E08-025 [51] off the neutron, currently under analysis. The exclusive kinematics proposed here for DVCS also allow for making measurements of the L/T separated exclusive π^0 cross section in a larger kinematic range, providing a constraint on σ_L and σ_T. If σ_T is confirmed to be large this could subsequently allow for a detailed investigation of transversity GPDs [49]. Conversely, the separated longitudinal cross section could allow for probing the usual GPDs through neutral pion production.

The measurement will be done in parallel with the DVCS measurement by detecting in coincidence scattered electrons in the existing HMS and photons from the decay of neutral pions using the Neutral Particle Spectrometer (NPS) [52]. The NPS will detect photons corresponding to π^0 electroproduction close to the direction of $\vec{q}$, the exchanged virtual photon three-momentum transfer. The high luminosity spectrometer+calorimeter system of the HMS+NPS combination in Hall C is well suited for such a measurement. The magnetic spectrometers benefit from relatively small point-to-point uncertainties, which are crucial for meaningful L-T separations.

A large acceptance device such as CLAS12 is well suited for measuring pseudoscalar meson electroproduction over a large range of $-t$ and x_B [53]. Though the large azimuthal coverage allows for a good determination of the interference terms, the main constraint is the error amplification in the extraction of longitudinal and transverse components. The use of the HMS and NPS in Hall C is proposed here as their characteristics best address the experimental requirements, and the existing knowledge of the properties of the HMS is expected to allow for a well understood isolation of the longitudinal and transverse cross sections. The sensitivity of the measurement is illustrated in Fig. 3 showing the uncorrelated point-to-point uncertainty and correlated uncertainties listed in Table II.

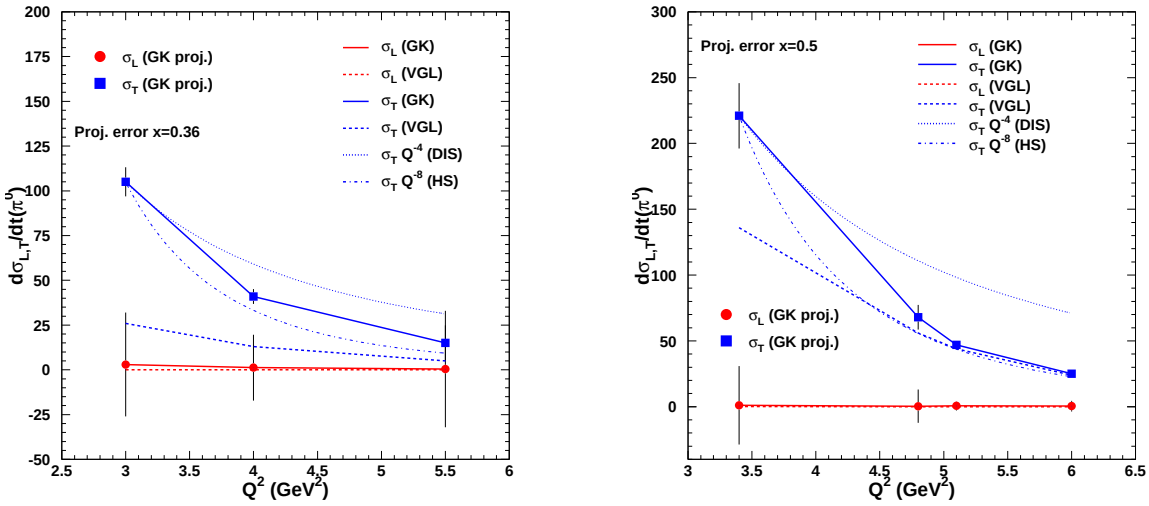

FIG. 3: Projected uncertainties for the Q^2 dependence of σ_L and σ_T at fixed x_B=0.36, 0.5. The points are plotted assuming the GK model predictions. Also shown are the hard scattering (HS, R=σ_L/σ_T $1/Q^{-2}$) and the DIS (DIS, R $1/Q^2$) expectation, and the model predictions of the VGL (Regge) model. The points at Q^2=5.1 and 6.0 GeV^2 in the right panel are scaled from the x_B=0.6 setting in Table III and include events from the Hall A DVCS experiment [28] for the low beam energy in the L/T separation where appropriate. The point at Q^2=5.5 GeV^2 also includes events from the Hall A experiment for the low beam energy in the L/T separation.

III. EXPERIMENTAL SETUP

We propose to make a precision coincidence setup measuring charged particles (scattered electrons or recoiling protons) with the existing HMS and photons using a $PbWO_4$ calorimeter [52].

To reduce electromagnetic backgrounds, we plan to use a conventional sweeping magnet, similar but with only $\sim 10\%$ of the field requirements of the Horizontal-Bend magnet presently under construction for the new Hall C/SHMS. This will enable us to achieve low-angle photon detection. Detailed background simulations show that this setup allows for $\geq 10\,\mu$A beam currents on a 10 cm long cryogenic LH2 target at the very smallest NPS angles, and much higher luminosities at larger γ, π^0 angles.

A. High Momentum Spectrometer

The magnetic spectrometers benefit from small point-to-point uncertainties, which are crucial for absolute cross section measurements such as those needed for meaningful Rosen-

bluth separations. In particular, the optical properties and the acceptance of the HMS have been studied extensively and are well understood in the kinematic range between 0.5 and 5 GeV, as evidenced by more than 200 L/T separations ($\sim$1000 kinematics) [54]. The position of the elastic peak has been shown to be stable to better than 1 MeV, and the precision rail system and rigid pivot connection have provided reproducible spectrometer pointing for about a decade.

B. Photon detection: the neutral particle spectrometer

We will construct a general-purpose and remotely rotatable neutral particle detection system for Hall C. A floor layout of the HMS and the proposed rotatable neutral-pion detection system is shown in Fig. 4(a). This neutral-pion detection system consists of the following elements:

- A sweeping magnet providing 0.3 T·m field strength, with similar outer geometry as the Horizontal-Bend (HB) Magnet presently under construction for the SHMS but with conventional copper coils.
- A neutral particle detector consisting of 1116 $PbWO_4$ blocks (similar to the PRIMEX [55] experimental setup, see Fig. 4(b)) in a temperature controlled frame, comprising a 25 msr device at a distance of 4 meters.
- Essentially deadtime-less digitizing electronics to independently sample the entire pulse form for each crystal allowing for background subtraction and identification of pile-up in each signal. This is a major improvement over the existing PRIMEX apparatus.
- A new set of high-voltage distribution bases with built-in amplifiers for operation in high-rate environments.
- Cantilevered platforms on the SHMS carriage, to allow for precise and remote rotation around the Hall C pivot of the full detection system, over an angle range between 5.5 and 30 degrees.
- A dedicated beam pipe with as large critical angle as possible to reduce backgrounds beyond the HB-type sweeping magnet.

To provide space for this sweeping magnet, the HB magnet for the SHMS needs to be removed. The HB adds a 3-degree horizontal pre-bend to the SHMS to allow reaching the smallest angles, as compared to an 18-degree vertical bend. Thus, it only provides a small perturbation to the SHMS optics, and as such removing and reinstalling the HB magnet does not impact the final SHMS optics understanding, given proper attention to alignment. In fact, the SHMS is in this sense comparable to the earlier SOS optics, where removing and properly reinstalling and realigning the SOS quadrupole did not imply additional work to understand the optics beyond the standard sieve-slit calibration runs.

(a) (b)

FIG. 4: (a) The DVCS/π^0 detector in Hall C. The cylinder at the top center is the (1 m diameter) vacuum chamber containing the 10 cm long liquid-hydrogen target. The long yellow tube emanating from the scattering chamber on the lower right is the downstream beam pipe. To the left of the beam pipe is the HMS. Only the liquid He and liquid N_2 lines for the large superconducting quadrupoles at the entrance to the spectrometer are clearly visible. To the right of the beam line, the first quadrupole of the SHMS and its cryogenic feed lines are shown. This spectrometer will be used as a carriage to support the $PbWO_4$ calorimeter (shown in its light-tight and temperature control box next to the beam line) and the associated sweep magnet. (b) The high resolution $PbWO_4$ part of the HYCAL [56] on which the present design is based.

The sweeping magnet will be a conventional version of the HB magnet presently under construction, with copper coils to effectively use the full bore of such a magnet (35 by 36 cm^2). In sharp contrast to the superconducting HB magnet, which provides a field strength of 1.93 T·m, we only require a 0.3 T·m field to sweep away charged particles up to 300 MeV/c. This modest field requirement is well within the range of conventional magnet coils, which alleviates the need for additional cryogenic and inner vacuum cans. The sweeping magnet design is matched to existing JLab power supplies and existing commercial conductors. The materials for the coil, 24 m of copper conductor of dimension 0.5 x 0.5 in^2, including a 1/4-

inch diameter water cooling channel, could be obtained from, for instance, Luvata-Finnland. The coil winding tools could be obtained through AES-Penn. The materials for the yoke steel could be obtained from vendors like Oakland Steel and would be purchased in slabs of 4" for easier machining in university machine shops. These magnet-component vendors also supplied the respective components for the Hall A PREX magnet. The estimated radiation dose at the location of the magnet ($<$ 30,000 rem/hr) was folded into decisions for radiation hard resins and insulation systems.

The obvious advantage of using a sweeping magnet cloning the geometric properties of the HB magnet is that it has a relatively large bore, of 35 by 36 cm^2, and is designed from the start to reach small scattering angles without impacting the main electron beam. The effective gap for an HB-type magnet for neutral particles may be slightly reduced, as the coil assumes a 3-degree horizontal pre-bend for charged particles. Thus, if we assume a direct clone of the HB the effective gap for neutral particles (assuming symmetric acceptance around the detection angle) is reduced to about 30 by 36 cm^2. This problem likely gets alleviated for a conventional magnet but we have assumed the latter aperture for the rate estimates. We found that we can move the "HB-clone" sweeping magnet about 20 cm forward as compared to the HB, such that the magnetic center is at a distance of 1.57 m from the pivot. This then constitutes a solid angle of 25.5 msr, with $\sim$146 mrad horizontal and $\sim$175 mrad vertical acceptance (taking into account a vacuum can of 1 meter length).

The $PbWO_4$ electromagnetic calorimeter

The energy resolution of the photon detection is the limiting factor of the experiment. Exclusivity of the reaction is ensured by the missing mass technique (see Section III D) and the missing-mass resolution is dominated by the energy resolution of the calorimeter.

Given the high luminosity and low angle of the detector in the planned experiment, radiation hardness is one essential factor when choosing the detector material. Two common choices for this kind of detection requirements are PbF_2 and $PbWO_4$. Table I summarizes the main properties of each of them. DVCS experiments with CLAS have used a $PbWO_4$ calorimeter [30]. In Hall A, however, a PbF_2 calorimeter was chosen as the photon detector. This choice was mainly driven by its fast time response and the fact that PbF_2 is a pure Čerenkov material, and thus insensitive to low energy background. The missing mass

Parameter	Lead Tungsten ($PbWO_4$)	Lead Fluoride (PbF_2)
Density (g/cm3)	8.28	7.66-7.77
Radiation length Xo (cm)	0.89	0.93-0.95
Refraction index	2.36 (λ = 420 nm) 2.24 (λ = 600 nm)	1.8-2.0 (depending on λ)
Transmission range (nm)	340-1000	250 -- 1100
Moliere radius (cm)	2.19	2.22
Radiation type Sensitivity to low en. bckgr.	Scintillation (~13% Čerenkov) Sensitive	Pure Čerenkov Insensitive (no scintillation)
Timing property (slow/fast) τ_{sc}, ns (%)	≈30 ns / 10 ns 5 (73%) 14 (23%) 110 (4%)	Very fast, Total pulse width < 20 ns
Lead content (% by weight)	> 85	85
Hydroscopicity	No	No
Energy resolution σ_E/E (%)	~2.4/$\sqrt{E}$	5.3/$\sqrt{E}$
Position resolution σ (mm)	~2.5/$\sqrt{E}$	~1.5/$\sqrt{E}$
Photon yields per 1 MeV	~140-200	~1.0-2.0
Temperature dependence of Light Yield	~ -2%/°C at room temperature	No need of temperature stabilization
Critical Energy (MeV)	--	8.6--9.0

TABLE I: Properties of PbF_2 and $PbWO_4$ crystals.

resolution will be only slightly affected by pile-up events and low energy background.

Nevertheless, results from Hall A experiments using PbF_2, together with a slightly different setup in Hall C, drive us to choose $PbWO_4$ for this new experiment. Firstly, Hall A results show that the energy resolution of the calorimeter is not so much dominated by the background (pile-up events and low energy particles), but is mainly due to the fluctuations in the number of Čerenkov photons. During Hall A experiment E00-007 [29] we recorded a sample of background events in the calorimeter using a random trigger. Fig. 5 shows the missing mass resolution obtained from a Monte Carlo simulation of our PbF_2 calorimeter including the background measured during the experiment. The missing mass resolution is $\sigma(M_X^2) = 0.096$ GeV^2, which is far from the resolution measured in the data for that particular kinematic setting $\sigma(M_X^2) = 0.182\,\mathrm{GeV}^2$. In order to match the resolution of the data, the simulation needs to be further smeared to account for the fluctuations of the number of Čerenkov photons collected. As shown in Table I, $PbWO_4$ has a much better light yield

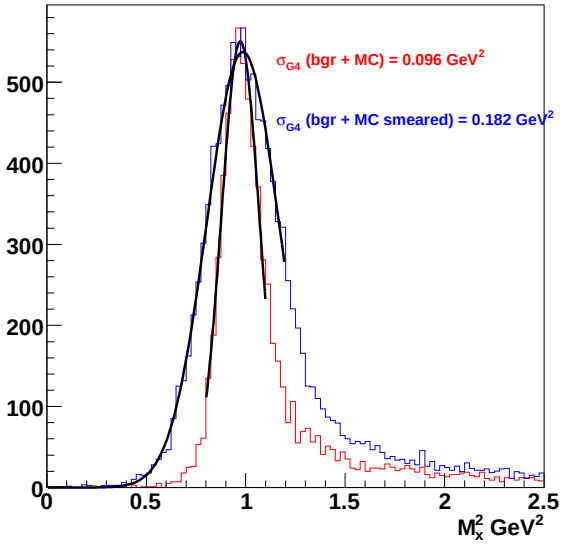

FIG. 5: Simulation of the missing mass resolution of PbF_2 with *real* background measured in Hall A experiment E07-007 (red). In order to match the resolution of the data, the simulation needs to be smeared assuming 175 photons/GeV were collected by PMTs (blue).

than PbF_2 and an intrinsic energy resolution twice better. Moreover, the use of a sweeping magnet in Hall C will reduce very significantly the background coming from low energy electrons.

We plan to use a $PbWO_4$ calorimeter 58 cm wide and 70 cm high. This corresponds to 29 by 34 $PbWO_4$ crystals of 2.05 by 2.05 cm^2 (each 18.0 cm long). We have added one crystal on each side to properly capture showers, and thus designed our $PbWO_4$ calorimeter to consist of 31 by 36 $PbWO_4$ crystals, or 64 by 74 cm^2. This amounts to a requirement of 1116 $PbWO_4$ crystals, less than the 1152 used in the Hybrid Calorimeter of the PRIMEX experiment.

To reject very low-energy background, a thin absorber could be installed in front of the $PbWO_4$ detector. The space between the sweeper magnet and the proximity of the $PbWO_4$ detector will be enclosed within a vacuum channel (with a thin exit window, further reducing low-energy background) to minimize the decay photon conversion in air.

The emission of $PbWO_4$ includes up to three components, and increases with increasing wave length: τ_1 ~5 ns (73%); τ_2 ~14 ns (23%) for emission of λ in the range of 400-550 nm; τ_3 has a lifetime more than 100 ns, but it is only ~4% of the total intensity. The light yield and the decay time of the $PbWO_4$ are temperature dependent, with the light yield

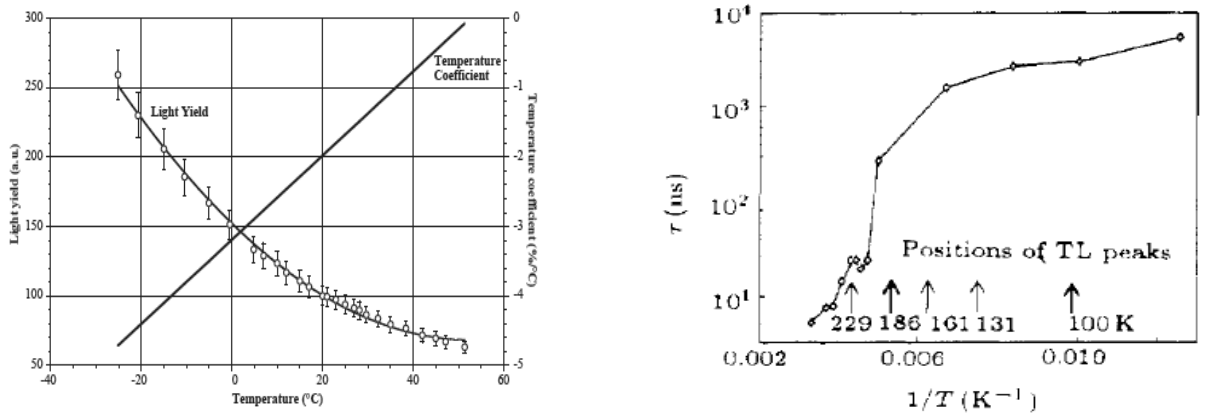

(a) (b)

FIG. 6: Temperature dependence of the light yield (a) and the decay time of the emission of the λ=400 nm light (b) for the crystal $PbWO_4$. Figure (a) adopted from P. Lecoq et al. [57–59], and (b) from Shi Chao-Shu, Chin [60].

increasing at low temperature (Fig. 6(a)), but the decay time (drastically) decreasing with temperatures near room temperature, as illustrated in Fig. 6(b).

Given the temperature sensitivity of the scintillation light output of the $PbWO_4$ crystals, the entire calorimeter must be kept at a constant temperature, to within 0.1° to guarantee 0.5% energy stability for absolute calibration and resolution. The high-voltage dividers on the PMTs may dissipate up to several hundred Watts, and this power similarly must not create temperature gradients or instabilities in the calorimeter. The calorimeter will thus be thermally isolated and be surrounded on all four sides by water-cooled copper plates. This design is based on that of the HYCAL temperature controlled frame and optimized with more recent experience from CMS [61], which has shown stability to 0.05° C. The materials for the frame are foreseen to include steel and steel alloy plates, copper plates, and a temperature control system, and the design accommodates a geometrical arrangement in an array of 36 by 31 crystals. A similar system has also operated successfully in the $PbWO_4$ calorimeter of CLAS, built by part of our group [62].

At the anticipated background rates, pile-up and the associated baseline shifts can adversely affect the calorimeter resolution, thereby constituting the limiting factor for the beam current. The solution is to read out a sampled signal, and perform offline shape analysis using a flash ADC (fADC) system. New HV distribution bases with built-in pre-amplifiers will allow for operating the PMTs at lower voltage and lower anode currents, and thus protect the photocathodes or dynodes from damage from the accumulated anode charge.

The $PbWO_4$ crystals are 2.05 x 2.05 cm^2. The typical position resolution is 2-3 mm. Each crystal covers 5 mrad, and the expected angular resolution is 0.5-0.75 mrad, which is comparable with the resolutions of the HMS and SOS, routinely used for Rosenbluth separations in Hall C. This can also be compared with the CLAS Inner Calorimeter (IC), which has crystals of dimensions 1.33 x 1.33 cm^2 at the front face and located at a distance of 0.55 m from the target. The CLAS IC has reached an angular resolution of 3-4 mrad [30]. Note that as compared to the CLAS IC the solid angle per crystal reduces in our case by a factor of 2.1.

To take full advantage of the high-resolution crystals while operating in a high-background environment, modern flash ADCs will be used to digitize the signal. They continuously sample the signal every 4 ns, storing the information in an internal FPGA memory. When a trigger is received, the samples in a programmable window around the threshold crossing are read out for each crystal that fired. Since the readout of the FPGA does not interfere with the digitizations, the process is essentially deadtime free.

C. Beam pipe and angle coverage

The major sources contributing to the dose in this experiment are the target-induced rates themselves and apertures of the beam line, where large-thickness materials such as vacuum flanges are at the closest (critical) distance from the beam. The incident beam will scatter in the target, and (multiple) scattering products will hit such narrow sections first. Subsequently, they will locally deposit almost their full energy in the beam pipe in the form of an electromagnetic cascade, irradiating a forward angular cone. To minimize this background, a conical or telescopic design of the initial portion of the beam exit line would be useful. This requirement routinely conflicts with the physics need to put the active detectors or spectrometers at forward angles.

Obviously, it is optimal to make the opening or critical angle for the beam exiting the target/scattering chamber region as large as possible.

For instance, if the critical angle would flare out to that determined by the two-feet diameter last section of the beam exit line far downstream, about a degree, then the main cone of scattered electrons would remain inside the vacuum pipe until well beyond the envisioned active detector and detector background. This way, the general background in

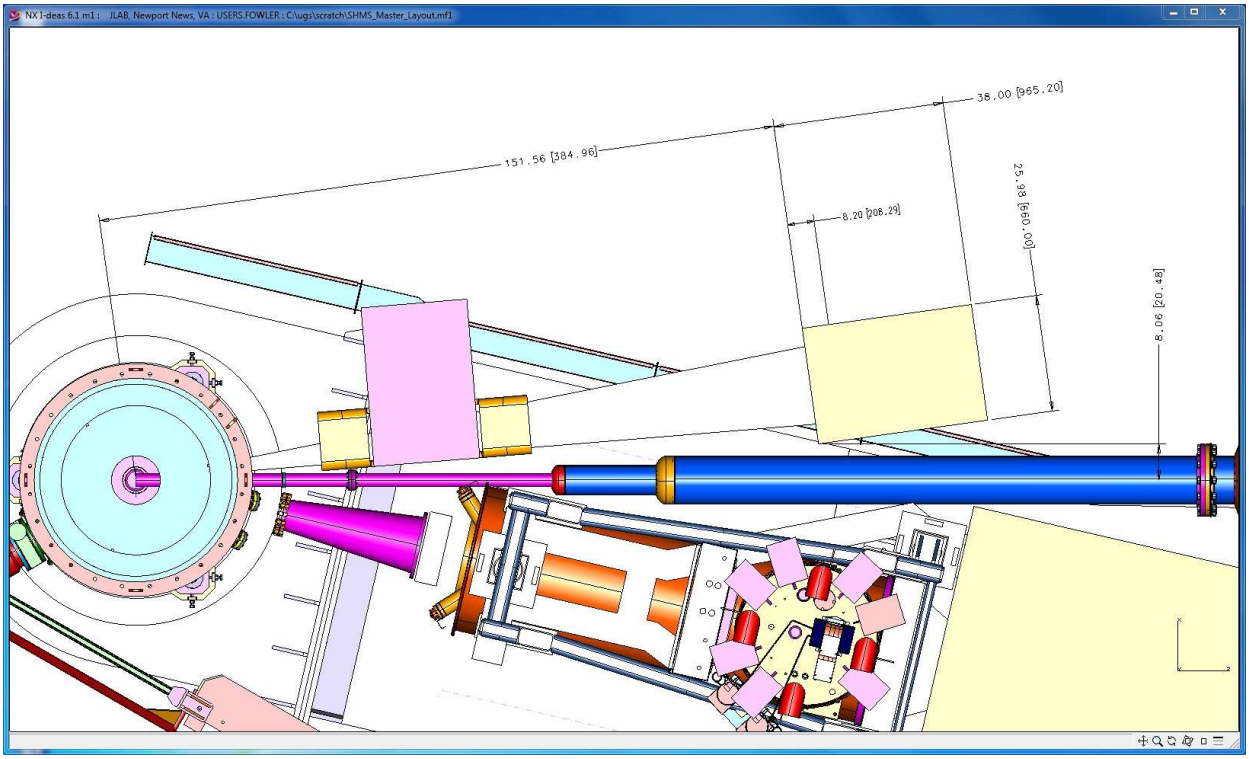

FIG. 7: Modified beam pipe assembly for the beam dump line. The initial beam pipe has a 2.5 inch diameter up to a distance of 2.35 m, just beyond the area where HMS-Q1 has a slot. Then, the beam pipe has a short section with 6 inch diameter, followed by a long 12-inch diameter section. With this beam pipe, the critical angle will be 13.5 mr. The HMS can rotate to 10.5 degrees (albeit only locally below 13 degrees), and NPS can reach its foreseen smallest angles.

the Hall will be significantly decreased, typically by a few 10's of % at higher beam energies, although much larger at lower beam energies.

The present "standard" critical angle for the Hall C configuration allowing for the smallest spectrometer angles (the so-called "small-angle beam pipe assembly") amounts to an 8.6 mr critical angle, induced by a two-inch diameter beam pipe up to a distance (from the pivot) of 2.96 m. The so-called "large-angle beam pipe" has a two-inch diameter beam pipe to only 1.45 m instead, and thus reaches a critical angle of 17.5 mr, nearly matched to the optimal flare of 1 degrees. However, the HMS can only reach a 15-degree scattering angle with this "large-angle beam pipe" assembly. The reason is that the HMS-Q1 (at a distance of a bit beyond 1.5 m) has a slot on the beam axis side, with a vertical dimension of 2.9 inches.

Hence, we plan to design a beam pipe with 2.5 inch diameter up to a distance of 2.35 m (beyond the slot in HMS-Q1), then flaring out to a larger diameter. This modified beam pipe assembly is illustrated in Fig. 7. It allows the HMS to achieve its smallest scattering

angle of 10.5°, albeit at the cost of sacrificing remote rotation for HMS below 13° or so, as the beam pipe fits snug into the HMS-Q1 slot. The modified beam pipe assembly does allow the NPS to reach its design smallest angle of 5.5° (equivalent to the smallest angle reach of SHMS) for a distance to the $PbWO_4$ calorimeter of 4 m. With this modified beam pipe assembly, we will achieve a critical angle of 13.5 mr. Note that this is the critical angle corresponding to the background simulations presented later. The general background for beam energies of 6 GeV and higher is, for this beam pipe assembly, dominated (90%) by the background generated directly in the beam-target interactions. Additional shielding can be considered between the beam line and the $PbWO_4$ calorimeter, near the critical distance.

More details on the NPS instrumentation can be found in our technical document [52].

D. Exclusivity of the DVCS and π^0 reactions

The exclusivity of the DVCS reaction will be based on the missing mass technique, successfully used during Hall A experiment E00-110. Fig. 8 presents the missing mass squared obtained in E00-110 for $H(e,e'\gamma)X$ events, with coincident electron-photon detection. The missing mass resolution achieved in the π^0 channel $H(e,e'\pi^0)X$ was superior [37]. After subtraction of an accidental coincidence sample, our data is essentially background free: we have negligible contamination of non-electromagnetic events in the HRS and PbF_2 spectra. In addition to $H(e,e'\gamma)p$, however, we do have the following competing channels: $H(e,e'\gamma)p\gamma$ from $ep \to e\pi^0 p$, $ep \to e\pi^0 N\pi$, $ep \to e\gamma N\pi$, $ep \to e\gamma N\pi\pi \ldots$. From symmetric (lab-frame) π^0-decay, we obtain a high statistics sample of $H(e,e'\pi^0)X'$ events, with two photon clusters in the PbF_2 calorimeter. From these events, we determine the statistical sample of [asymmetric] $H(e,e'\gamma)\gamma X'$ events that must be present in our $H(e,e'\gamma)X$ data. The M_X^2 spectrum displayed in black in Fig. 8 was obtained after subtracting this π^0 yield from the total (green) distribution. This is a 14% average subtraction in the exclusive window defined by 'M_X^2 cut' in Fig. 8. Depending on the bin in $\phi_{\gamma\gamma}$ and t, this subtraction varies from 6% to 29%. After our π^0 subtraction, the only remaining channels, of type $H(e,e'\gamma)N\pi$, $N\pi\pi$, *etc.* are kinematically constrained to $M_X^2 > (M+m_\pi)^2$. This is the value ('M_X^2 cut' in Fig. 8) we chose for truncating our integration. Resolution effects can cause the inclusive channels to contribute below this cut. To evaluate this possible contamination, during E00-110 we used an additional proton array (PA) of 100 plastic scintillators. The PA sub-

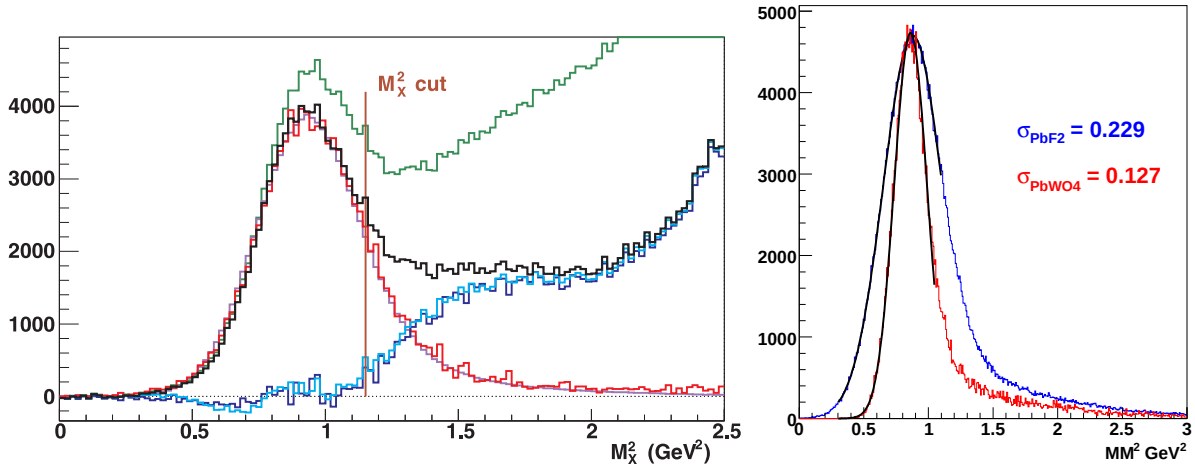

FIG. 8: Left: Missing mass squared in experiment E00-110 for H$(e,e'\gamma)X$ events (green curve) at $Q^2 = 2.3$ GeV^2 and $-t \in [0.12, 0.4]$ GeV^2, integrated over the azimuthal angle of the photon $\phi_{\gamma\gamma}$. The black curve shows the data once the H$(e,e'\gamma)\gamma X'$ events have been subtracted. The other curves are described in the text. Right: Projected missing mass resolution for a similar kinematic setting ($E_b = 6.6$ GeV, $Q^2 = 3$ GeV^2, $x_B = 0.36$). By using $PbWO_4$ instead of PbF_2, the missing mass resolution will be considerably improved. Values are given in Table III and are to be compared to the value $\sigma(M_X^2) = 0.2$ GeV^2 obtained in previous experiments in Hall A and shown in this figure (Left).

tended a solid angle (relative to the nominal direction of the **q**-vector) of $18^\circ < \theta_{\gamma p} < 38^\circ$ and $45^\circ < \phi_{\gamma p} = 180^\circ - \phi_{\gamma\gamma} < 315^\circ$, arranged in 5 rings of 20 detectors. For H$(e,e'\gamma)X$ events near the exclusive region, we can predict which block in the PA should have a signal from a proton from an exclusive H$(e,e'\gamma p)$ event. The red histogram is the $X = (p + y)$ missing mass squared distribution for H$(e,e'\gamma p)y$ events in the predicted PA block, with a signal above an effective threshold 30 MeV (electron equivalent). The blue curve shows our inclusive yield, obtained by subtracting the normalized triple coincidence yield from the H$(e,e'\gamma)X$ yield. The (smooth) violet curve shows our simulated H$(e,e'\gamma)p$ spectrum, including radiative and resolution effects, normalized to fit the data for $M_X^2 \leq M^2$. The cyan curve is the estimated inclusive yield obtained by subtracting the simulation from the data. The blue and cyan curves are in good agreement, and show that our exclusive yield has less than 2% contamination from inclusive processes.

In this proposed experiment we plan to use a $PbWO_4$ calorimeter with a resolution better than twice the resolution of the PbF_2 calorimeter used in E00-110. While the missing mass resolution will be slightly worse at certain high beam energy, low x_B kinematics, the better energy resolution of the crystals will largely compensate for it, and the missing mass

Source	pt-to-pt (%)	scale (%)
Acceptance	0.4	1.0
Electron PID	<0.1	<0.1
Efficiency	0.5	1.0
Electron tracking efficiency	0.1	0.5
Charge	0.5	2.0
Target thickness	0.2	0.5
Kinematics	0.4	<0.1
Exclusivity	1.0	2.0
π^0 subtraction (for DVCS)	0.5	1.0
Radiative corrections	1.2	2.0
Total	1.8–1.9	3.8–3.9

TABLE II: Estimated systematic uncertainties for the proposed experiment based on previous Hall C and Hall A experiments.

resolution in this experiment will be significantly better than ever before. Fig. 8 (Right) shows the missing mass resolution for PbF_2 and $PbWO_4$ for a kinematic setting similar to the one measured in Hall A. Table III shows the missing mass resolution projected for each of the settings using the proposed $PbWO_4$ calorimeter.

E. Systematics uncertainties

The HMS is a very well understood magnetic spectrometer which will be used here with modest requirements (beyond the momentum), defining the (x_B, Q^2) kinematics well. Table II shows the estimated systematic uncertainties for the proposed experiment based on previous experience from Hall C equipment and Hall A experiments. The uncorrelated errors between high and low ϵ settings are listed in the first column. The point-to-point uncertainties are amplified by $1/\Delta\epsilon$ in the beam energy separation. The scale uncertainties propagate directly into the separated cross sections.

IV. PROPOSED KINEMATICS AND PROJECTIONS

Table III provides the kinematics and beam time requested. The first set of kinematic points will provide a beam energy dependence of the cross section at fixed Q^2 and x_B. These settings complement the Hall A approved settings with one additional beam energy and two where possible. Additionally, three settings are proposed at identical kinematics as the ones approved in Hall A. This will provide a consistency check between the two different experimental setups. The combined time for this cross-check is 3 days. The last set of settings in Table III corresponds to the high Q^2 and low x_B extension. The total amount of beam time requested is 65 days.

	Energy Dependence at fixed (Q^2, $x_{\rm B}$)												Low-$x_{\rm B}$				High-Q^2		
$x_{\rm B}$	0.36					0.50			0.60				0.2				0.36	0.50	0.60
Q^2 (GeV)^2	3.0			4.0		3.4		4.8	5.1			6.0	2.0			3.0	5.5	8.1	10
k (GeV)	6.6*	8.8	11	8.8*	11	8.8	11	11	6.6	8.8*	11	11	6.6	8.8	11	11	11		
k' (GeV)	2.2	4.4	6.6	2.9	5.1	5.2	7.4	5.9	2.1	4.3	6.5	5.7	1.3	3.5	5.7	3.0	2.9	2.4	2.1
$\theta_{\rm Calo}$ (deg)	11.7	14.7	16.2	10.3	12.4	20.2	21.7	16.6	13.8	17.8	19.8	17.2	6.3	9.2	10.6	6.3	7.9	8.0	8.0
$D_{\rm Calo}$ (m)	3	3	3	4	3	3	3	3	3	3	3	3	6	4	4	6	4	4	4
$I_{\rm beam}$ (μA)	28	28	28	50	28	28	28	28	28	28	28	28	11	5	50	11	50	50	50
$\rm N_{evt}$ (10^5)	1.5	8.8	8.2	2.1	7.9	7.3	11	5.1	0.2	0.2	2.7	2.6	3.5	3.6	64	3.4	6.1	0.8	0.4
$\sigma_{M_X^2}$(GeV^2)	0.13	0.13	0.12	0.15	0.15	0.09	0.09	0.11	0.09	0.09	0.09	0.09	0.17	0.17	0.17	0.22	0.19	0.15	0.13
Days	1	2	1	1	3	3	2	5	5	1	5	10	1	1	1	1	5	5	12

TABLE III: DVCS and π^0 kinematics for Hall C. The incident and scattered beam energies are k and k', respectively. The calorimeter is centered at the angle $\theta_{\rm Calo}$, which is set equal to the nominal virtual-photon direction. The front face of the calorimeter is at a distance $D_{\rm Calo}$ from the center of the target, and it is adjusted to optimize multiple parameters: First to maximize acceptance, second to ensure sufficient separation of the two clusters from symmetric $\pi^0 \to \gamma\gamma$ decays, and third to ensure that the edge of the calorimeter is never at an angle less than 3.2° from the beam line. The row $I_{\rm beam}$ shows the beam current and $N_{\rm evt}$ is the number of DVCS counts expected integrated over $\phi_{\gamma\gamma}$ in a bin in t of width 0.1 GeV^2 (at $t_{\rm min}$). The three settings marked by * in the beam energy row correspond to cross checks with Hall A kinematics.

The different kinematic settings are represented in Fig. 9 in the Q^2–x_B plane. The area below the straight line $Q^2 = (2M_pE_b)x_B$ corresponds to the physical region for a maximum

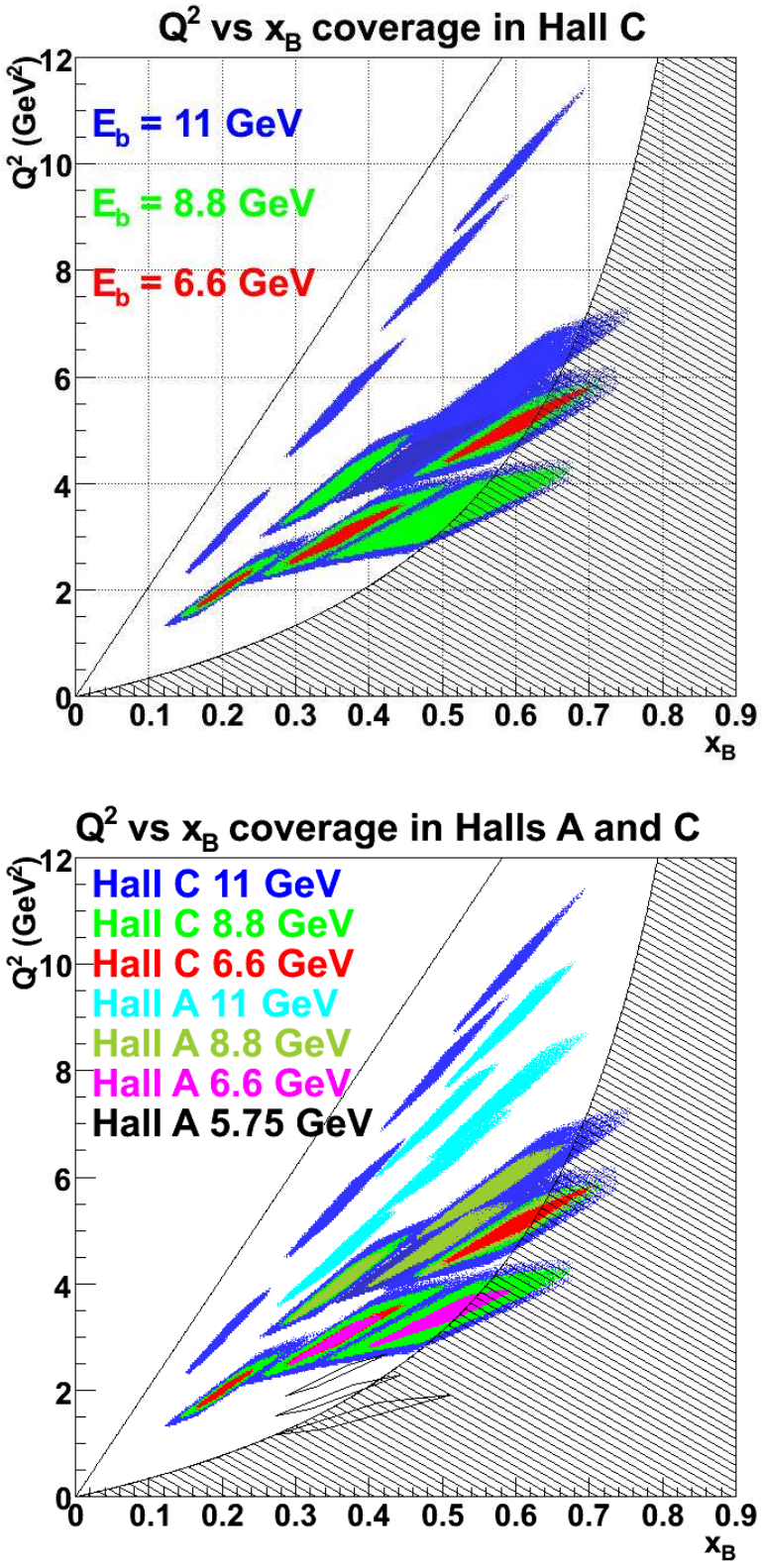

FIG. 9: Display of different kinematic setting proposed. Different colors correspond to different beam energies. The top plot shows the proposed settings in Hall C (this experiment), whereas the bottom plots displays the combined coverage between the Hall A and Hall C programs. Shaded areas show the resonance region $W < 2$ GeV and the line $Q^2 = (2M_pE_b)x_B$ limits the physical region for a maximum beam energy $E_b = 11$ GeV.

beam energy $E_b = 11$ GeV. Also plotted is the resonance region $W < 2$ GeV. As one can observe almost the full accessible domain is covered by the proposed experiment, and this at different beam energies, each one represented by a different color. For comparison, the lower plot in Fig. 9 shows the combined coverage between Hall A E12-06-114 and the proposed experiment.

We have performed detailed Monte Carlo simulation of the experimental setup and evaluated counting rates for each of the settings. In order to do this, we have used a recent global fit of world data with LO sea evolution by D. Müller and K. Kumerički [63]. This fit reproduces the magnitude of the DVCS cross section measured in Hall A at $x_B = 0.36$ and is available up to values of $x_B \leq 0.5$. For our high x_B settings we used a GPD parameterization fitted to Deeply Virtual Meson Production data [64], together with a code to compute DVCS cross sections, provided by H. Moutarde [65, 66]. Notice that for DVCS, counting rates and statistical uncertainties will be driven *at first order* by the Bethe-Heitler (BH) cross section, which is well-known.

Fig. 10 shows the projected results for one of the beam-energy-separation settings ($x_B = 0.5$ and $Q^2 = 3.4$ GeV^2). The top plot shows the cross-section measurements at $E_b = 8.8$ GeV, the middle plot shows them at $E_b = 11$ GeV, and the bottom row shows the cross sections after subtraction of the pure BH cross section, represented by the red lines in the cross-section plots. Statistical uncertainties are shown by error bars, and systematic uncertainties are represented by the cyan bands. One can see the high statistical precision on the variation of the unpolarized cross section with beam energy. This kinematic difference allows us to separate the real part of the BH-DVCS interference from the DVCS^2 terms of the cross section. Notice also that the imaginary part of the BH-DVCS interference will be obtained with great statistical precision from the helicity difference of cross sections at each beam energy. In this case, any beam-energy dependence of the helicity-dependent cross section is a signature of twist-three DVCS^2 terms. The beam-time request for these two settings is 3 days (8.8 GeV) and 2 days (11 GeV).

Fig. 11 shows one of the settings of our proposed low-x_B extension, at $Q^2 = 3$ GeV^2. Due to the high counting rates of these settings, we can obtain very high statistical accuracy with only 1 day of beam time. The top row shows the unpolarized cross section as a function of $\phi_{\gamma\gamma}$ for several bins in t, compared to the BH cross section shown in red. The bottom row displays the cross-section difference for opposite beam helicities. The BH process is expected

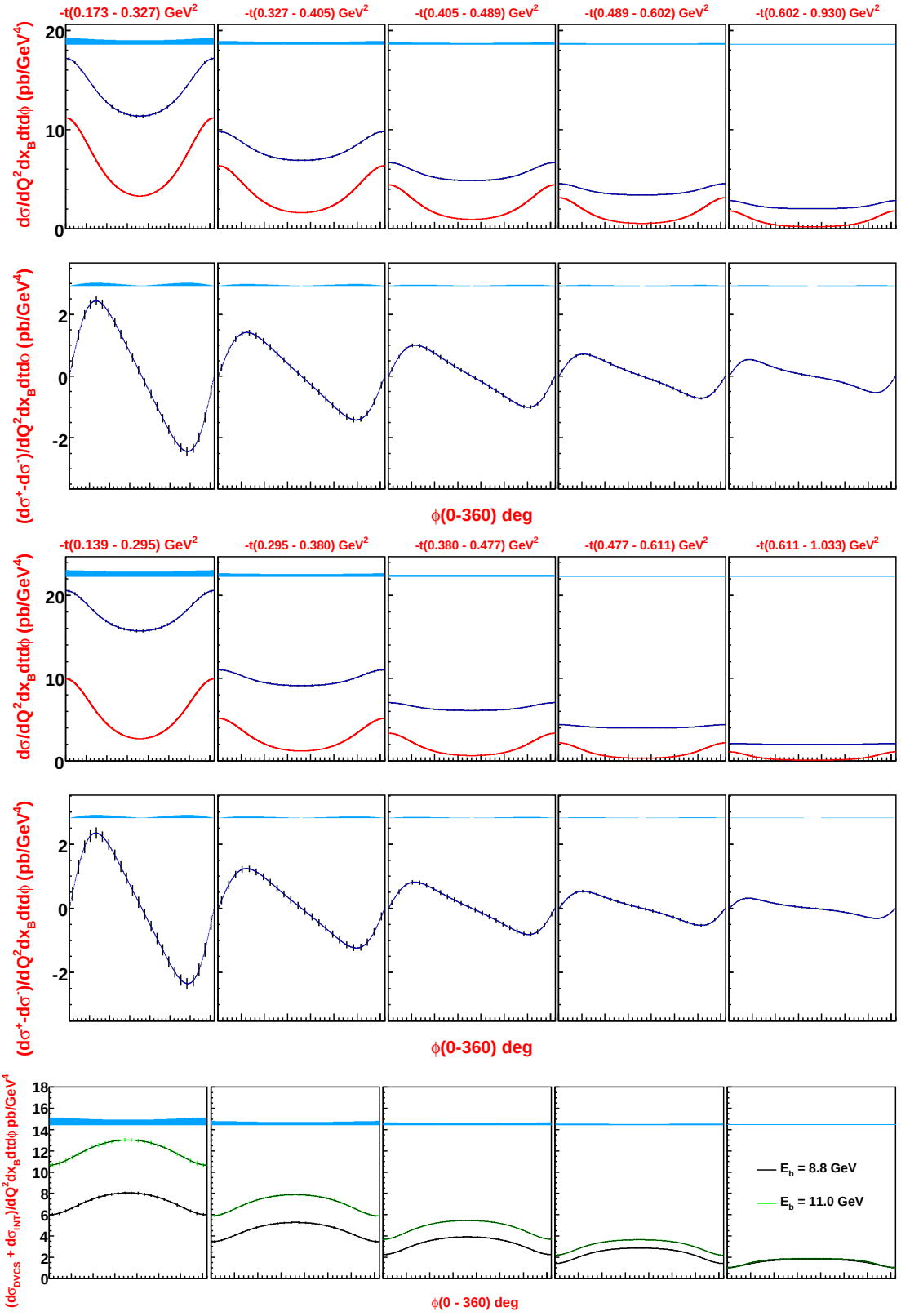

FIG. 10: Rosenbluth separation for the two settings at $x_B = 0.5$ and $Q^2 = 3.4$ GeV^2. The top two plots show the cross-section measurements at $E_b = 8.8$ GeV, the middle plots show them at $E_b = 11$ GeV and the bottom row shows the two cross sections after subtraction from BH. Cross-section differences for opposite beam-helicities are also shown.

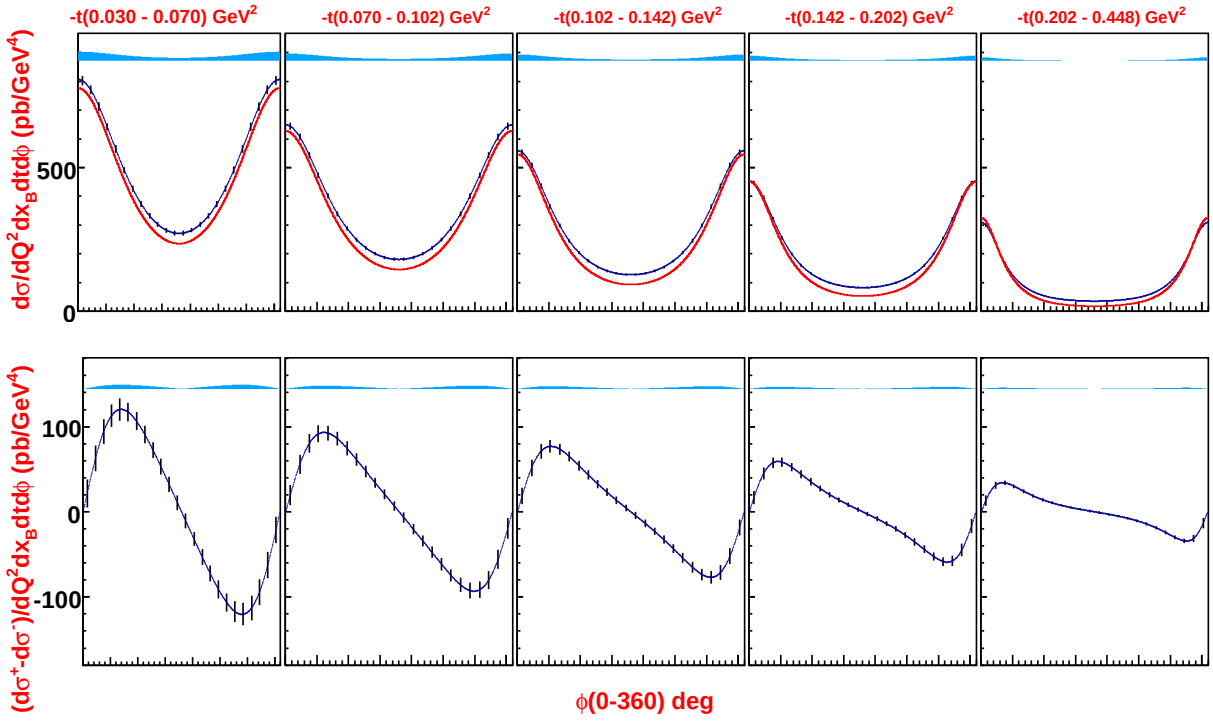

FIG. 11: Low-x_B setting at $Q^2 = 3\,\mathrm{GeV}^2$, $x_B = 0.2$. Top plot is the unpolarized cross section, with the $|\mathrm{BH}|^2$ contribution in red. Bottom plot is the beam helicity-dependent cross section.

to dominate the unpolarized cross-section at this kinematics. The helicity dependent cross section, sensitive to the imaginary part of the DVCS-BH interference will be measured with high statistical precision.

Finally, Fig. 12 shows two of our high-Q^2-extension settings. Obviously, these settings require more time, but as can be seen in the projections, we can obtain very reasonable statistics with 5 and 12 days of beam, respectively.

V. BACKGROUND STUDIES

We have made detailed Monte Carlo studies of the backgrounds that will illuminate the calorimeter in this experiment. These studies are based on the DINREG code (GEANT3) of P. Degtiarenko. The background in the calorimeter limits the luminosity in two ways. First, the total absorbed dose can cause radiation damage to the crystals, whose primary consequence is to diminish the photon yield from the high-energy showers. Second, fluctuations in the high energy component of the background will degrade the event-by-event energy and position resolution of the calorimeter, this aspect was discussed in a previous section.

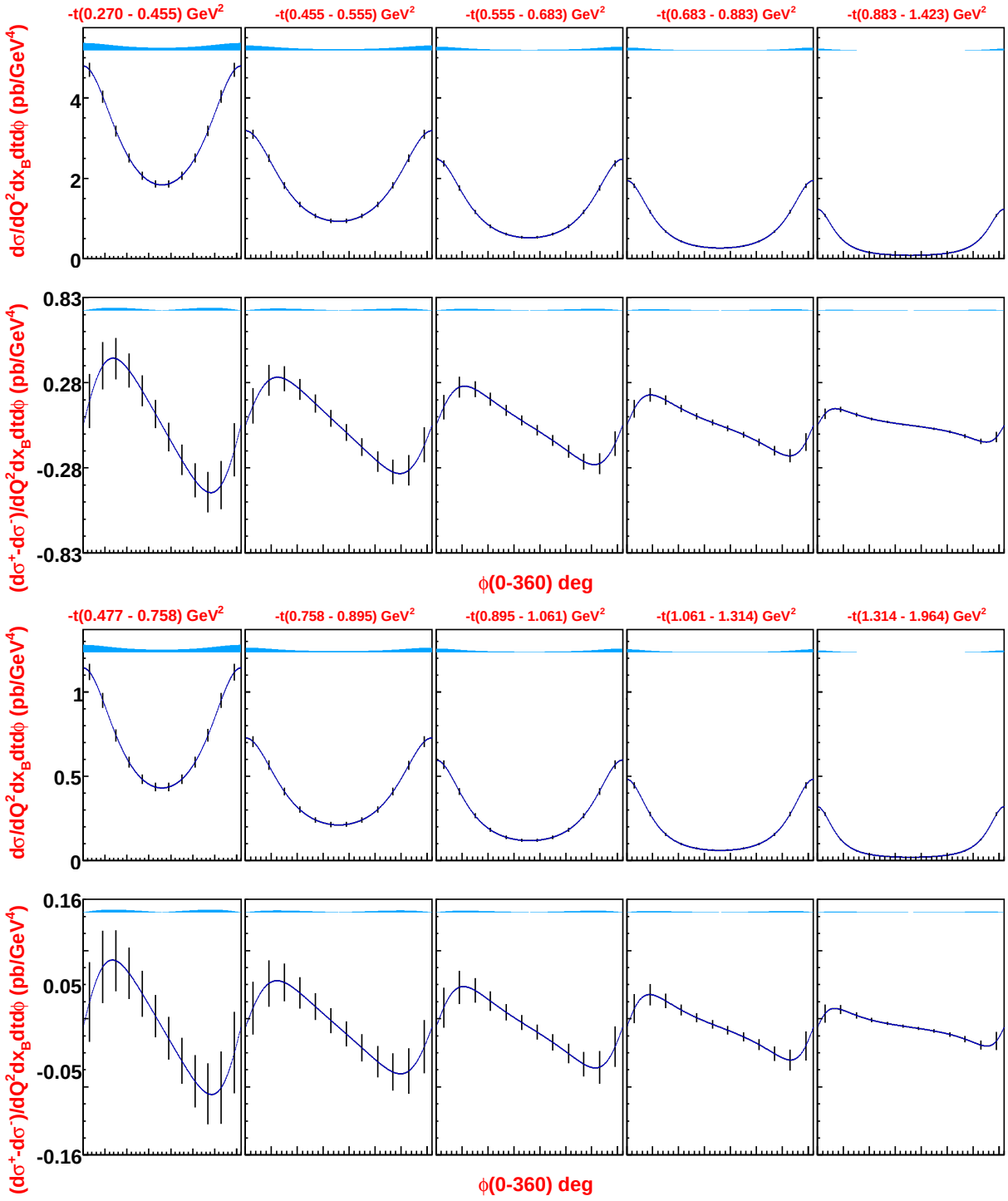

FIG. 12: Projections for the highest Q^2 settings: $Q^2 = 8$ GeV^2 (top, $x_B = 0.5$) and $Q^2 = 10$ GeV^2 (bottom, $x_B = 0.6$).

The essential results from the background simulation are that the background is primarily electromagnetic and is primarily line-of-sight from the target (as opposed to secondary scattering from the downstream beam pipe). These conclusions lead us to propose a ~ 0.3

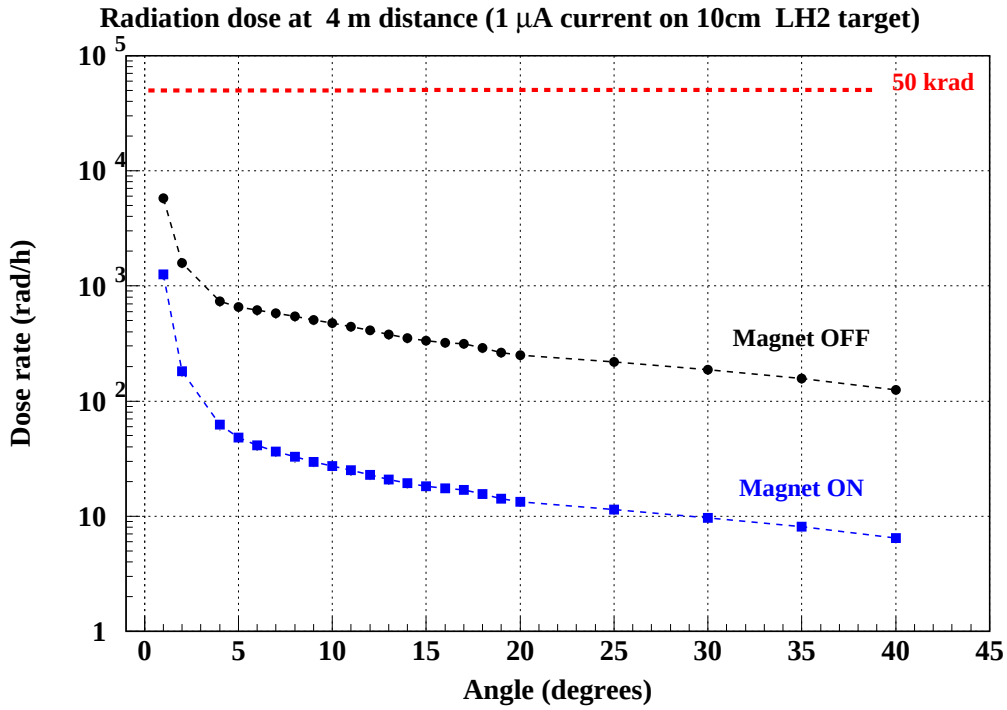

FIG. 13: Dose rates *vs.* angle for the $PbWO_4$ calorimeter. Dose is calculated for 1 μA incident on a 10 cm liquid H_2 target, with the calorimeter 4 m from the target. A dose of 50 kRad (0.5 Gray) is presumed to be the limiting dose before curing of the calorimeter is required.

Tesla-m sweep magnet in between the target and the spectrometer. This will effectively remove the dominant electron background for $p_e \leq 300\,\mathrm{MeV/c}$. This will be a horizontal bend magnet with an aperture optimized to match the acceptance of the calorimeter and to allow central calorimeter angles as small as 6.3°.

The background dose to individual crystals in the calorimeter, as a function of angle from the beamline, is illustrated in Fig. 13. Our previous experience with a high luminosity calorimeter is with PbF_2 in Hall A. PbF_2 and $PbWO_4$ have similar radiation hardness. We have completed two experiments in Hall A with an unshielded calorimeter. Each experiment had an illumination of ~ 500 hrs at a luminosity of $10^{37}/\mathrm{cm}^2/\mathrm{s}$, equivalent to $\sim 4\,\mu$A incident on a 10 cm target. For at least half of the beam hours, the calorimeter crystal closest to the beamline was at 7°. In each experiment, we experienced 10-20% diminishing of the signal yield per GeV, but no other consequences of radiation damage. Upon visual inspection of the crystals, visual damage was limited to a yellowing of the first 1-2 cm of the crystal. This is consistent with the damage being primarily caused by low energy background, and the damage having limited impact on the energy resolution, since the bulk of the light emission is

at 'shower-max' around 4-5 cm into the crystals. Furthermore, the damage is self-annealing when the crystals are left un-irradiated for a period of months.

Fig. 13 illustrates that the sweep magnet will reduce the background dose by roughly a factor of 10 for angles $> 10^\circ$. For angles as small as 3°, the suppression is still a factor of 5. In fact, a crystal at 3° with the magnet on will see less total radiation than the closest crystals (7°) in the Hall A experiments (without sweep magnet). Based on the Hall A results, and the simulation summarized in Fig. 13, we project a luminosity that will scale as

$$\mathcal{L} = \left[10^{37}\,\mathrm{cm}^{-2}\mathrm{sec}^{-1}\right] \frac{D_{\mathrm{Calo}}^2}{(1.1\,\mathrm{m})^2}\,, \tag{10}$$

where D_{Calo} is the calorimeter distance in Table III, and 1.1 m is the calorimeter distance in the previous Hall A experiments.

VI. SUMMARY

We propose to measure the cross section of the DVCS reaction accurately in a wide range of kinematics allowed by a set of beam energies up to 11 GeV. We will exploit the azimuthal angle, beam energy and helicity dependence of the cross section to extract the complete set of observables from an unpolarized proton target. The Q^2 dependence of each individual term will be measured and compared to the predictions of the handbag mechanism. This will provide a quantitative estimate of higher-twist effects to the GPD formalism in JLab kinematics.

Many of the proposed settings will be run at different beam energies. This will permit to separate the BH-DVCS interference from the DVCS^2 terms of the unpolarized cross section. At the same time we will also perform an L/T separation of the exclusive π^0 electroproduction cross section, also as a function of Q^2.

We plan to use the Hall C High-Momentum Spectrometer combined with a high resolution $PbWO_4$ electromagnetic calorimeter.

In order to complete this full mapping of the DVCS and exclusive π^0 cross section over the wide range of kinematics, we request 65 days of longitudinally polarized electron beam ($\mathcal{P} > 75\%$, with only a few percent transverse polarization).

Appendix A: DVCS Formalism

The bilinear DVCS Fourier coefficients are:

$$
\begin{aligned}
c_0^{DVCS} &= 2\frac{2-2y+y^2+\frac{\epsilon^2}{2}y^2}{1+\epsilon^2}\mathcal{C}^{DVCS}(\mathcal{F},\mathcal{F}^*)+\frac{16K^2}{(2-x_B)^2(1+\epsilon^2)}\mathcal{C}^{DVCS}(\mathcal{F}_{\text{eff}},\mathcal{F}^*_{\text{eff}}) \\
\begin{Bmatrix} c_1^{DVCS} \\ \lambda s_1^{DVCS} \end{Bmatrix} &= \frac{8K}{(2-x_B)(1+\epsilon^2)}\begin{Bmatrix} 2-y \\ -\lambda y\sqrt{1+\epsilon^2} \end{Bmatrix}\begin{Bmatrix} \Re\text{e} \\ \Im\text{m} \end{Bmatrix}\mathcal{C}^{DVCS}(\mathcal{F}^{eff},\mathcal{F}^*)\,, \qquad \text{(A1)}
\end{aligned}
$$

where $\mathcal{F}$ represents the set $\{\mathcal{H},\,\mathcal{E},\,\widetilde{\mathcal{H}},\,\widetilde{\mathcal{E}}\}$ of twist-2 CFFs and $\mathcal{F}_{\text{eff}}$ represents the higher-twist matrix elements.

The Fourier coefficients $c_n^{\mathcal{I}}$ and $s_n^{\mathcal{I}}$ of the interference term are:

$$
\begin{aligned}
c_n^{\mathcal{I}} &= C_{++}(n)\Re\text{e}\,\mathcal{C}^{\mathcal{I}}_{++}(n|\mathcal{F})+C_{0+}(n)\Re\text{e}\,\mathcal{C}^{\mathcal{I}}_{0+}(n|\mathcal{F}_{\text{eff}})\,, \\
s_n^{\mathcal{I}} &= S_{++}(n)\Im\text{m}\,\mathcal{S}^{\mathcal{I}}_{++}(n|\mathcal{F})+S_{0+}(n)\Im\text{m}\,\mathcal{S}^{\mathcal{I}}_{0+}(n|\mathcal{F}_{\text{eff}})\,. \qquad \text{(A2)}
\end{aligned}
$$

The above coefficients are defined in terms of the photon helicity-conserving

$$
\begin{aligned}
\mathcal{C}^{\mathcal{I}}_{++}(n|\mathcal{F}) &= \mathcal{C}^{\mathcal{I}}(\mathcal{F})+\frac{C^V_{++}(n)}{C_{++}(n)}C^{\mathcal{I},V}(\mathcal{F})+\frac{C^A_{++}(n)}{C_{++}(n)}\mathcal{C}^{\mathcal{I},A}(\mathcal{F}) \\
\mathcal{S}^{\mathcal{I}}_{++}(n|\mathcal{F}) &= \mathcal{C}^{\mathcal{I}}(\mathcal{F})+\frac{S^V_{++}(n)}{S_{++}(n)}C^{\mathcal{I},V}(\mathcal{F})+\frac{S^A_{++}(n)}{S_{++}(n)}\mathcal{C}^{\mathcal{I},A}(\mathcal{F}) \qquad \text{(A3)}
\end{aligned}
$$

and helicity-changing amplitudes

$$
\begin{aligned}
\mathcal{C}^{\mathcal{I}}_{++}(n|\mathcal{F}_{\text{eff}}) &= \frac{\sqrt{2}}{2-x_B}\frac{\widetilde{K}}{Q}\left[\mathcal{C}^{\mathcal{I}}(\mathcal{F}_{\text{eff}})+\frac{C^V_{++}(n)}{C_{++}(n)}C^{\mathcal{I},V}(\mathcal{F}_{\text{eff}})+\frac{C^A_{++}(n)}{C_{++}(n)}\mathcal{C}^{\mathcal{I},A}(\mathcal{F}_{\text{eff}})\right] \\
\mathcal{S}^{\mathcal{I}}_{++}(n|\mathcal{F}_{\text{eff}}) &= \frac{\sqrt{2}}{2-x_B}\frac{\widetilde{K}}{Q}\left[\mathcal{C}^{\mathcal{I}}(\mathcal{F}_{\text{eff}})+\frac{S^V_{++}(n)}{S_{++}(n)}C^{\mathcal{I},V}(\mathcal{F}_{\text{eff}})+\frac{S^A_{++}(n)}{S_{++}(n)}\mathcal{C}^{\mathcal{I},A}(\mathcal{F}_{\text{eff}})\right]. \qquad \text{(A4)}
\end{aligned}
$$

The complete expressions of kinematic coefficients $C_{ab}(n)$, $S_{ab}(n)$ and $\widetilde{K}$ are given in [36], and their beam energy dependence will be exploited here in order to disentangle all possible terms of the cross section.

In conclusion, at leading twist there are 3 linear combinations and 1 bilinear combination

of CFFs entering the DVCS cross-section:

$$
\begin{aligned}
\mathcal{C}^{\mathcal{I}}(\mathcal{F}) &= F_1\mathcal{H} - \frac{t}{4M^2}F_2\mathcal{E} + \frac{x_B}{2-x_B+x_B\frac{t}{Q^2}}(F_1+F_2)\widetilde{\mathcal{H}}\,, \\
\mathcal{C}^{\mathcal{I},V}(\mathcal{F}) &= \frac{x_B}{2-x_B+x_B\frac{t}{Q^2}}(F_1+F_2)(\mathcal{H}+\mathcal{E})\,, \\
\mathcal{C}^{\mathcal{I},A}(\mathcal{F}) &= \frac{x_B}{2-x_B+x_B\frac{t}{Q^2}}(F_1+F_2)\widetilde{\mathcal{H}}\,, \\
\mathcal{C}^{\rm DVCS}(\mathcal{F},\mathcal{F}^*) &= \frac{Q^2(Q^2+x_Bt)}{((2-x_B)Q^2+x_Bt)^2}\Bigg\{4(1-x_B)\mathcal{H}\mathcal{H}^* + 4\left(1-x_B+\frac{2Q^2+t}{Q^2+x_Bt}\frac{\epsilon^2}{4}\right)\widetilde{\mathcal{H}}\widetilde{\mathcal{H}}^* \\
&- \frac{x_B^2(Q^2+t)^2}{Q^2(Q^2+x_Bt)}(\mathcal{H}\mathcal{E}^*+\mathcal{E}\mathcal{H}^*) - \frac{x_B^2Q^2}{Q^2+x_Bt}(\widetilde{\mathcal{H}}\widetilde{\mathcal{E}^*}+\mathcal{E}\mathcal{H}^*) \\
&- \left(\frac{x_B^2(Q^2+t)^2}{Q^2(Q^2+x_Bt)} + \frac{((2-x_B)Q^2+x_Bt)^2}{Q^2(Q^2+x_Bt)}\frac{t}{4M^2}\right)\mathcal{E}\mathcal{E}^* \\
&\qquad -\frac{x_B^2Q^2}{Q^2+x_Bt}t4M^2\widetilde{\mathcal{E}}\widetilde{\mathcal{E}}^*\Bigg\}\,,
\end{aligned}
\tag{A5}
$$

with 3 linear and 2 bilinear additional combinations at twist 3: $\mathcal{C}^{\mathcal{I}}(\mathcal{F}_{\rm eff})$, $\mathcal{C}^{\mathcal{I},V}(\mathcal{F}_{\rm eff})$, $\mathcal{C}^{\mathcal{I},A}(\mathcal{F}_{\rm eff})$, $\mathcal{C}^{\rm DVCS}(\mathcal{F}_{\rm eff},\mathcal{F}^*)$ and $\mathcal{C}^{\rm DVCS}(\mathcal{F}_{\rm eff},\mathcal{F}^*_{\rm eff})$.

REFERENCES

[1] D. Mueller, D. Robaschik, B. Geyer, F. M. Dittes, and J. Horejsi, Fortschr. Phys. **42**, 101 (1994), hep-ph/9812448.

[2] X.-D. Ji, Phys.Rev. **D55**, 7114 (1997), hep-ph/9609381.

[3] X.-D. Ji, Phys. Rev. Lett. **78**, 610 (1997), hep-ph/9603249.

[4] X.-D. Ji, W. Melnitchouk, and X. Song, Phys.Rev. **D56**, 5511 (1997), hep-ph/9702379.

[5] A. V. Radyushkin, Phys. Rev. **D56**, 5524 (1997), hep-ph/9704207.

[6] A. Radyushkin, Phys.Lett. **B380**, 417 (1996), hep-ph/9604317.

[7] A. V. Belitsky, D. Mueller, and A. Kirchner, Nucl. Phys. **B629**, 323 (2002), hep-ph/0112108.

[8] M. Burkardt (2007), 0711.1881.

[9] O. Teryaev (2005), hep-ph/0510031.

[10] I. Anikin and O. Teryaev, Phys.Rev. **D76**, 056007 (2007), 0704.2185.

[11] I. Anikin and O. Teryaev, Fizika **B17**, 151 (2008), 0710.4211.

[12] M. Diehl and D. Y. Ivanov (2007), 0712.3533.

[13] M. V. Polyakov and C. Weiss, Phys.Rev. **D60**, 114017 (1999), hep-ph/9902451.

[14] M. Guidal, H. Moutarde, and M. Vanderhaeghen, accepted in Rep. Prog. Phys. **76** (2013), hep-hp/1303.6600.

[15] M. Guidal, Eur.Phys.J. **A37**, 319 (2008), 0807.2355.

[16] H. Moutarde, Phys.Rev. **D79**, 094021 (2009), 0904.1648.

[17] M. Guidal and H. Moutarde, Eur.Phys.J. **A42**, 71 (2009), 0905.1220.

[18] M. Guidal, Phys.Lett. **B689**, 156 (2010), 1003.0307.

[19] M. Guidal, Phys.Lett. **B693**, 17 (2010), 1005.4922.

[20] K. Kumericki and D. Mueller, Nucl.Phys. **B841**, 1 (2010), 0904.0458.

[21] G. R. Goldstein, J. O. Hernandez, and S. Liuti, Phys.Rev. **D84**, 034007 (2011), 1012.3776.

[22] C. Mezrag, H. Moutarde, and F. Sabatié (2013), 1304.7645.

[23] H. Moutarde, B. Pire, F. Sabatie, L. Szymanowski, and J. Wagner, Phys.Rev. **D87**, 054029 (2013), 1301.3819.

[24] K. Kumericki, D. Muller, and A. Schafer, JHEP **1107**, 073 (2011), 1106.2808.

[25] C. Muñoz Camacho et al. (Jefferson Lab Hall A Collaboration, Hall A DVCS Collaboration),

Phys.Rev.Lett. **97**, 262002 (2006), nucl-ex/0607029.

[26] V. Braun, A. Manashov, and B. Pirnay, Phys.Rev.Lett. **109**, 242001 (2012), 1209.2559.

[27] X. Ji, X. Xiong, and F. Yuan, Phys.Rev.Lett. **109**, 152005 (2012), 1202.2843.

[28] J. Roche, C. E. Hyde-Wright, B. Michel and C. Muñoz Camacho (spokespersons), PR12-06-114, approved by PAC30 (2006), nucl-ex/0609015.

[29] C. Muñoz Camacho, P. Bertin, J. Roche, C. Hyde et al. (2007), experiment E07-007 (Hall A).

[30] F. Girod et al. (CLAS Collaboration), Phys.Rev.Lett. **100**, 162002 (2008), 0711.4805.

[31] H.-S. Jo, PoS **QNP2012**, 052 (2012), 1207.3709.

[32] F. Sabatié, A. Biselli, L. Elouadrhiri, W. Kim, D. Ireland, H. Egiyan, M. Holtrop et al. (2006), experiment E06-12-119 (Hall B).

[33] S. Niccolai, V.Kubarovsky, A. El Alaoui, M. Mirazita et al. (2011), experiment E12-11-003 (Hall B).

[34] F. Gautheron et al., COMPASS-II Proposal, CERN-SPSC-2010-014, SPSC-P-340, May 17,2010.

[35] M. Diehl, T. Gousset, B. Pire, and J. P. Ralston, Phys. Lett. **B411**, 193 (1997), hep-ph/9706344.

[36] A. Belitsky and D. Mueller, Phys.Rev. **D82**, 074010 (2010), 1005.5209.

[37] E. Fuchey, A. Camsonne, C. Munoz Camacho, M. Mazouz, G. Gavalian, et al., Phys.Rev. **C83**, 025201 (2011), 1003.2938.

[38] I. Bedlinskiy et al. (CLAS Collaboration), Phys.Rev.Lett. **109**, 112001 (2012), 1206.6355.

[39] J. C. Collins, L. Frankfurt, and M. Strikman, Phys.Rev. **D56**, 2982 (1997), hep-ph/9611433.

[40] S. J. Brodsky and G. R. Farrar, Phys.Rev.Lett. **31**, 1153 (1973).

[41] K. Park et al. (CLAS Collaboration), Eur.Phys.J. **A49**, 16 (2013), 1206.2326.

[42] A. Airapetian et al. (HERMES Collaboration), Phys.Lett. **B682**, 345 (2010), 0907.2596.

[43] R. De Masi et al. (CLAS Collaboration), Phys.Rev. **C77**, 042201 (2008), 0711.4736.

[44] T. Horn, X. Qian, J. Arrington, R. Asaturyan, F. Benmokthar, et al., Phys.Rev. **C78**, 058201 (2008), 0707.1794.

[45] S. Goloskokov and P. Kroll, Eur.Phys.J. **C65**, 137 (2010), 0906.0460.

[46] S. Goloskokov and P. Kroll, Eur.Phys.J. **A47**, 112 (2011), 1106.4897.

[47] P. Hoodbhoy and X.-D. Ji, Phys.Rev. **D58**, 054006 (1998), hep-ph/9801369.

[48] M. Diehl, Eur.Phys.J. **C19**, 485 (2001), hep-ph/0101335.

[49] P. Kroll (2012), π^0 *Electroproduction*, private communication.

[50] M. Gockeler et al. (QCDSF Collaboration, UKQCD Collaboration), Phys.Lett. **B627**, 113 (2005), hep-lat/0507001.

[51] M. Mazouz, P. Bertin, C. Hyde, A. Camsonne et al. (2008), experiment E08-025 (Hall A).

[52] NPS technical document, https://hallcweb.jlab.org/experiments/PAC40/NPS/nps.pdf.

[53] P. Stoler, K. Joo, M. Ungaro, C. Weiss, V. Kubarovsky et al. (2006), experiment E12-06-108 (Hall B).

[54] Y. Liang et al. (Jefferson Lab Hall C E94-110 Collaboration) (2004), nucl-ex/0410027.

[55] S. D. A. Gasparian et al. (2002), experiment E02-103 (Hall B).

[56] M. Kubantsev, I. Larin, and A. Gasparyan (PrimEx Collaboration), AIP Conf.Proc. **867**, 51 (2006), physics/0609201.

[57] P. Lecoq, I. Dafinei, E. Auffray, M. Schneegans, M. Korzhik, et al., Nucl.Instrum.Meth. **A365**, 291 (1995).

[58] E. Auffray, P. Lecoq, M. Korzhik, A. Annenkov, O. Jarolimek, et al., Nucl. Instrum. Meth. **A402**, 75 (1998).

[59] A. Annenkov, E. Auffray, A. Borisevich, G. Y. Drobyshev, A. Fedorov, et al., Nucl. Instrum. Meth. **A403**, 302 (1998).

[60] S. Chao-Shu et al., Chinese Phys. Lett. **15**, 455 (1998).

[61] G. Franzoni (CMS Collaboration), Nucl.Instrum.Meth. **A628**, 90 (2011).

[62] H. Jo, Ph.D. thesis, Université Paris-Sud, Orsay, France (2007).

[63] D. Müller and K. Kumerički, model 3: http://calculon.phy.pmf.unizg.hr/gpd/.

[64] P. Kroll, H. Moutarde, and F. Sabatie, Eur.Phys.J. **C73**, 2278 (2013), 1210.6975.

[65] H. Moutarde (2013), TGV code for fast calculation of DVCS cross sections from CFFs, private communication.

[66] P.A.M. Guichon and M. Vanderhaeghen (2008), Analytic $ee'\gamma$ cross section, in Atelier DVCS, Laboratoire de Physique Corpusculaire, Clermont-Ferrand, June 30 - July 01.